Invited Review Article: Instrumentation for nuclear magnetic resonance in zero and ultralow magnetic field

Michael C. D. Tayler,[1,2,a)] Thomas Theis,[3] Tobias F. Sjolander,[4] John W. Blanchard,[5] Arne Kentner,[6] Szymon Pustelny,[7] Alexander Pines,[4] and Dmitry Budker[1,8,9]
[1]*Department of Physics, UC Berkeley, Berkeley, California 94720, USA*
[2]*Department of Chemical Engineering and Biotechnology, Cambridge University, Cambridge, United Kingdom*
[3]*Department of Chemistry, Duke University, Durham, North Carolina 27708, USA*
[4]*College of Chemistry, UC Berkeley, Berkeley, California 94720, USA*
[5]*Helmholtz Institut Mainz, 55099 Mainz, Germany*
[6]*RWTH Aachen, Aachen, Germany*
[7]*Institute of Physics, Jagiellonian University, 30-348 Kraków, Poland*
[8]*Nuclear Sciences Division, Lawrence Berkeley National Laboratory, Berkeley, California 94720, USA*
[9]*Helmholtz Institut Mainz, Johannes Gutenberg Universität, Mainz, Germany*

(Received 9 May 2016; accepted 30 August 2017; published online 29 September 2017)

We review experimental techniques in our laboratory for nuclear magnetic resonance (NMR) in zero and ultralow magnetic field (below 0.1 μT) where detection is based on a low-cost, non-cryogenic, spin-exchange relaxation free ^{87}Rb atomic magnetometer. The typical sensitivity is 20-30 fT/Hz$^{1/2}$ for signal frequencies below 1 kHz and NMR linewidths range from Hz all the way down to tens of mHz. These features enable precision measurements of chemically informative nuclear spin-spin couplings as well as nuclear spin precession in ultralow magnetic fields. *Published by AIP Publishing.*
https://doi.org/10.1063/1.5003347

I. INTRODUCTION

Nuclear magnetic resonance (NMR) signals are commonly detected using inductive coupling,[1] where the sample is placed in a magnetic field (B) and the Larmor precession of the atomic nuclei induces an electromotive force (emf) in a nearby circuit. Inductive detection favors high magnetic fields because the emf is proportional to the magnetic field and the equilibrium nuclear spin polarization[2,3] is proportional to magnetic field, leading the NMR signal to noise ratio (SNR) to scale approximately as B^2.[3–7] High fields also increase chemical shift dispersion for experiments addressing specific nuclear spins and/or chemical environments.[8] At present, a top-of-the-range high-field NMR instrument with a 10-20 T superconducting magnet (approaching the GHz frequency regime) and a low-noise or cryo-cooled induction circuit[9] can be used for analyses of chemical samples down to the picomole level and of sample volumes around 1–10 μL.[10,11]

However, there are many applications of NMR for which there is a preference for detecting signals at low fields: (1) The study of samples containing phase boundaries and therefore large variations in magnetic susceptibility, e.g., mixed phases and porous materials, can be challenging in high fields. Spectral peaks are broad because of the induced inhomogeneity in the NMR magnetic field. In contrast, towards zero field, the broadening becomes small compared to the natural linewidth of the resonances.[12] (2) The NMR spectra of orientationally disordered samples, e.g., glassy or powdered solids, are broad at high fields due to the truncation of spin interactions by the imposed symmetry of the magnetic field. In low fields, where interactions with the external field are weak compared to spin-spin couplings, there is no truncation and spectra are sharp.[13–15] (3) For samples enclosed in metal containers, NMR signals can be strongly attenuated due to the skin-depth effect, which scales with the inverse square root of frequency. At 10 MHz in copper or aluminum, the penetration depth is around 20 μm; in contrast, at 1 kHz it is around 2 mm, deep enough to allow signals to pass through the walls of, say, a soda can.[16,17] (4) At zero field, spin coherences in liquids can persist for many tens of seconds, corresponding to ultra-narrow linewidths on the order of mHz. Such narrow lines can be used for chemical fingerprinting and precise measurement of spin-spin couplings.[18–25] Combined with the ease of obtaining highly homogeneous low fields, zero and ultralow magnetic field (ZULF) represents a facile route to chemically resolved NMR.

ZULF NMR demands instrumentation that is different to that from conventional NMR since inductive detection of the low-frequency signals is extremely time consuming.[26] In this paper, we review instrumentation for non-inductive NMR detection based on alkali-atom magnetometers.[27–31] These magnetometers measure the magnitude of magnetic field emanating from the NMR sample via the ground-state precession of angular momenta in vaporized alkali metal atoms, e.g., K, Rb, or Cs.[32–36] Alkali magnetometers are most sensitive at low fields owing to the alkali vapor becoming spin-exchange relaxation free (SERF) at fields below ~100 nT.[37–40] The fundamental sensitivity of SERF magnetometers is comparable to that of superconducting quantum interference devices (SQUIDs),[41,42] which until the advent of atomic magnetometers were the predominant means of detecting ZULF NMR signals[12,43,44] or ZULF magnetic resonance images.[45–47]

[a)]Electronic mail: mcdt2@cam.ac.uk

As a guideline, SQUID sensitivity surpasses that of an inductive coil for frequencies below 1-10 MHz, taking spin polarization, sample volume, and all other factors as equal.[48] Like for a SQUID, the sensitivity of an atomic magnetometer is broadly independent of detection frequency. However, the bandwidth is not as large. Depending on the design, SQUIDs can detect across several hundreds of kHz, but atomic magnetometers typically reach only a few hundreds of Hz down to a few Hz in the most sensitive SERF regime. On the other hand, ultralow-field NMR spectra of liquid-state samples containing only ^{1}H, ^{13}C, ^{19}F, or ^{15}N nuclei usually span less than 1 kHz, so in this application the limitation is not a major one. A highly attractive feature of atomic magnetometers with respect to SQUIDs is that they do not require cryogenic cooling—in fact, they operate at or above room temperature—and are therefore significantly less complex and costly. Other features, for example, a much smaller magnetic shield needed to obtain an ultralow field environment around the sensor, enable the atomic magnetometer apparatus to be compact and to fit on a laboratory benchtop while the shielding and other (e.g., cryostat) hardware associated with SQUIDs is presently much larger.

Over the past decade, SERF atomic magnetometers were applied, down to chip-scale,[49–51] in many situations where earth's field NMR has normally been used, e.g., hyperpolarized gas imaging,[52] spin relaxation and molecular diffusion measurement in the absence of resolved chemical shifts,[53] and the quantification of net spin order in strongly polarized samples.[54] They have also been extensively used to obtain NMR spectra with ultrahigh (mHz) resolution of the scalar spin-spin couplings in non-viscous liquids, where the measurement precision is typically an order of magnitude higher than that achieved using high-field NMR[19,55,56] and the measurement of spin-spin dipolar couplings in oriented gels.[15] Technical development of the magnetometers is presently in a stage of rapid advance also due to their use in many other scientific areas including biomagnetism[57] and fundamental physics.[58]

In Sec. II, we describe the appearance of NMR signals in ultralow and zero magnetic field. We then explain how these are measured by describing our apparatus in the chronological order of the experiment, which involves (1) polarization, (2) encoding, and (3) detection of the nuclear spins. The atomic magnetometer used in this work had a sensitivity of 3×10^{-14} T $\mathrm{Hz}^{-1/2}$, which is a compromise between bandwidth, sensitivity, and size. In Sec. III, details are given for building, calibrating, and then operating the instrument to perform NMR measurements. We conclude with a discussion of future development and possible improvements.

II. SPIN DYNAMICS AT ULTRALOW FIELD

The NMR spectrum is obtained by Fourier transformation of a time-domain signal from the magnetometer whose amplitude is proportional to the total nuclear magnetization of the NMR sample. We define the total magnetization along z as our measurable. This is a convenient yet arbitrary choice as is detailed further in Sec. III D. With this choice, the signal is given as

$$\mathrm{signal}(t) \propto \langle M_z \rangle(t) \equiv \sum_j h\gamma_j \langle I_z^{(j)} \rangle / 2\pi. \tag{1}$$

In the above expression, $\langle M_z \rangle$ is the ensemble-averaged magnetization of the sample along the z-axis, which equates to the total expectation value of angular momentum, $\langle I_z^{(j)} \rangle$, for each nucleus j in the system multiplied by its gyromagnetic ratio, γ_j.

For convenience, we set $h = 1$ and measure energies in Hz. The time dependence of $\langle M_z \rangle$ is computed in the density matrix formalism from the trace over the operator product $M_z\rho(t)$, where $\rho(t)$ is the nuclear spin density matrix operator for the sample. The nuclear spin Hamiltonian, $H(t)$, determines the time-dependence of $\rho(t)$ by propagation. In the case where H is time-independent and spin relaxation is ignored, the result is

$$\langle M_z \rangle(t) = \mathrm{Tr}(M_z^{\dagger} \exp[-2\pi \mathrm{i} H t] \rho(0) \exp[+2\pi \mathrm{i} H t]). \tag{2}$$

We shall give three basic instances of this equation to illustrate the NMR phenomenon at ultralow magnetic fields. The first is the Larmor precession of magnetically equivalent nuclei with spin quantum number $I = 1/2$ in the presence of an applied field $\boldsymbol{B} = \{B_x, B_y, B_z\}$ (e.g., the ^{1}H nuclei in a sample of water, oil, or ethanol). In this instance, the Hamiltonian is $H = (\gamma/2\pi)\boldsymbol{I}^{(j)} \cdot \boldsymbol{B}$, where $\boldsymbol{I}^{(j)} = \{I_x^{(j)}, I_y^{(j)}, I_z^{(j)}\}$ and the exponential parts of Eq. (2) correspond to a rotation operator $R = \exp[-\mathrm{i}\gamma(\boldsymbol{I}^{(j)} \cdot \boldsymbol{B})t]$; the spins precess about the axis of the applied field at an angular velocity $\gamma\boldsymbol{B}$ and $\rho(t) = R\rho(0)R^{-1}$. Thus, if ^{1}H magnetization is initially prepared along the z axis and a magnetic field is applied along the x axis, ($|\boldsymbol{B}| = B_x$, $B_y = 0$, $B_z = 0$), the result will be $\langle M_z \rangle(t) = \langle M_z \rangle(0) \cos(\gamma_{\mathrm{H}} B_x t)$. This NMR experiment is itself a form of magnetometry as the value of B_x can be deduced from the measured signal frequency.

An example of the above is shown in Fig. 1(a). A spectrum was recorded using the atomic magnetometer for a 100 μL sample of tap water in a field along the x axis, produced by a current of 0.3 mA applied to a wire solenoid surrounding the sample; the value of the gyromagnetic ratio is $\gamma_{\mathrm{H}} = 2.675 \times 10^{8}$ rad s^{-1} T^{-1}, therefore the signal at $|\gamma_{\mathrm{H}} B_x / 2\pi|$ = 2.3 Hz corresponds to precession in the field of the coil, around $B_x = 5.40 \times 10^{-8}$ T. The initial condition in the experiment was polarization of the spins along the z axis at a level of approximately 7 ppm, achieved by placing the sample in the field of a permanent magnet (2 T) located approximately 20 cm away from the magnetometer followed by rapid shuttling into the low-field region. Further details on this protocol, including the coil dimensions and geometry, are given in Secs. III A and III B.

In this case, the magnetometer is sensitive to the projection of field along a single axis and the sign of the precession frequency cannot be determined. To determine the sign, quadrature detection would be needed, which could be realized using two magnetometers, the second sensitive to fields along the x or y axis.

Nuclear spin-coherence lifetime and magnetic field homogeneity determine the precision to which B_x can be measured since both of these parameters influence the linewidth of the spectral peak. For the water sample in Fig. 1(a), the lifetime

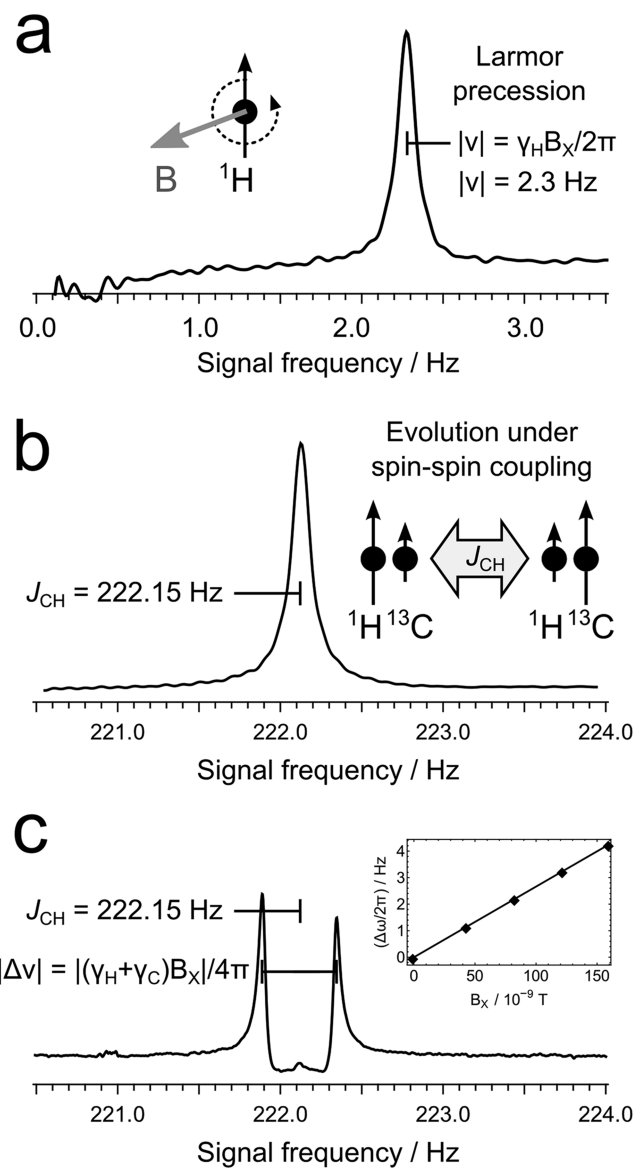

FIG. 1. Examples of low-frequency NMR signals detected at ultralow fields: (a) the Larmor precession of water in a bias field ~54 nT applied perpendicular to the detection axis (x and z axes, respectively); (b) measurement of the carbon-hydrogen spin-spin scalar coupling in [^{13}C]-formic acid in the absence of a bias field ("zero field"); (c) near-zero-field NMR signals of [^{13}C]-formic acid where the field direction is the same as that applied in (a). The Zeeman interaction is perturbative relative to the spin-spin coupling, causing splittings that are symmetrical about the zero-field transition.

(≈4 s) is the dominant factor. More precise measurements of field magnitude $|\boldsymbol{B}|$ can be achieved using other nuclei, e.g., ^{3}He and ^{129}Xe. Although these nuclei have relatively low gyromagnetic ratios ($\gamma_{^3\mathrm{He}} \approx 0.76\gamma_\mathrm{H}$ and $\gamma_{^{129}\mathrm{Xe}} \approx 0.28\gamma_\mathrm{H}$, respectively), they can sustain coherence lifetimes on the order of hours due to the chemical inertness of the atoms. Strong signals can be obtained through spin-exchange optical-pumping techniques.[59,60] The measurements of precession can be precise enough for navigation-grade gyroscopes.[61]

The second instance of Eq. (2) concerns systems of coupled nuclear spins. The NMR spectrum of a liquid is also a function of the indirect dipole-dipole couplings between the nuclear spins, which are mediated by the molecular electrons and described by a term in the intramolecular Hamiltonian $H_J = \sum_{j,k>j} J_{jk}\boldsymbol{I}^{(j)} \cdot \boldsymbol{I}^{(k)}$. A simple system illustrating this is [^{13}C]-formic acid (H^{13}COOH) in zero field. The spin system is assumed to comprise the spin-1/2 pair involving the ^{13}C and ^{1}H nuclei on the formyl group (the acidic ^{1}H undergoes rapid chemical exchange and can be ignored). This leads to $H = H_J = J_\mathrm{CH}(I_x^\mathrm{H}I_x^\mathrm{C} + I_y^\mathrm{H}I_y^\mathrm{C} + I_z^\mathrm{H}I_z^\mathrm{C})$. We have defined "zero field" as where the Larmor frequencies are much smaller than both the inverse of the spin coherence time and the spin-spin couplings, so the Zeeman interaction is dropped from the Hamiltonian.

The coupling constant $J_\mathrm{CH} = 222.15$ Hz results in a peak in the zero-field spectrum, as shown in Fig. 1(b). In a similar way to our example of ^{1}H Larmor precession in water, the signal arises when the starting nuclear spin density operator $\rho(0)$ does not commute with H. One such operator is $\rho(0) = k(I_z^\mathrm{H} - I_z^\mathrm{C})$, where k is a constant. The set of operators $A_1 = (I_x^\mathrm{H}I_x^\mathrm{C} + I_y^\mathrm{H}I_y^\mathrm{C})$, $A_2 = (I_z^\mathrm{H} - I_z^\mathrm{C})/2$, and $A_3 = (I_x^\mathrm{H}I_y^\mathrm{C} - I_y^\mathrm{H}I_x^\mathrm{C})$ obey the commutation relationship $[A_1, A_2] = \mathrm{i}A_3$ plus cyclic permutations $[A_2, A_3] = \mathrm{i}A_1$ and $[A_3, A_1] = \mathrm{i}A_2$ and in addition $[A_1, A_4] = [A_2, A_4] = [A_3, A_4] = 0$ with $A_4 = I_z^\mathrm{H}I_z^\mathrm{C}$. These allow one to use the standard result $\exp[-\mathrm{i}\theta(A_1 + A_4)]A_2 \exp[+\mathrm{i}\theta(A_1 + A_4)] = A_2\cos\theta + A_3\sin\theta$ to evaluate Eq. (2) given the initial condition and reach the result $\rho(t) = k[(I_z^\mathrm{H} - I_z^\mathrm{C})\cos(2\pi J_\mathrm{CH}t) + (2I_x^\mathrm{H}I_y^\mathrm{C} - 2I_y^\mathrm{H}I_x^\mathrm{C})\sin(2\pi J_\mathrm{CH}t)]$. It is then deduced that $\langle M_z\rangle(t) = \langle M_z\rangle(0)\cos(2\pi J_\mathrm{CH}t)$; the magnetization oscillates at the frequency J_CH. Details for the preparation of $\rho(0)$ may be found in Secs. III B and III C.

More generally the appearance of the ZULF NMR spectra can be determined by expanding Eq. (2) in terms of matrix elements between the normalized eigenstates $\{|\psi_j\rangle\}$ of H,

$$\langle M_z\rangle(t) = \sum_{k>j,j} \langle\psi_j|\rho(0)|\psi_k\rangle\langle\psi_j|M_z|\psi_k\rangle \exp(-2\pi\mathrm{i}\nu_{jk}t). \quad (3)$$

The exponents contain the eigenfrequencies, i.e., energy differences between eigenstates, denoted by $\nu_{jk} \equiv (\langle\psi_j|H|\psi_j\rangle - \langle\psi_k|H|\psi_k\rangle)$. The appearance of the NMR spectra for more than two coupled spins is extensively discussed in the literature.[19,23,25] As a general rule, oscillatory signals are not detectable if the detection operator M_z commutes with H. Any two matrix operators that commute have the same eigenstates. Thus, the matrix elements $\langle\psi_j|M_z|\psi_k\rangle$ are zero for $|\psi_j\rangle \neq |\psi_k\rangle$ because $|\psi_k\rangle$ are eigenstates of M_z and are orthonormal ($\langle|\psi_j|\psi_k\rangle = \delta_{jk}$). Although matrix elements $\langle\psi_j|M_z|\psi_j\rangle$ can be nonzero, the transition frequency is zero and so the rule holds. For a system at zero field, where all of the spins have the same gyromagnetic ratio, M_z and H_J always commute. It can be concluded that detection of the zero-field spectrum therefore requires coupling between more than one spin species in the system.

While the frequencies of the ultralow-field NMR signals can be predicted exactly using the eigenvalue-eigenvector approach [Eq. (3)], for fields below 0.1 μT the Zeeman interaction is small enough to be treated as a first-order perturbation to the zero-field eigensystem.[21] When a bias field is applied along the x or y axis, transitions in the NMR spectrum appear split into $n = 2(2F + 1)$ equal-spaced components corresponding to $\Delta m_F = \pm 1$ for each m_F, where F and m_F are the quantum numbers of $|F, m_F\rangle$, the lower-angular-momentum eigenstate of the two involved (for the construction of these quantum

numbers, see Refs. 21 and 25). As demonstrated in Fig. 1(c), the ~222 Hz transition in [^{13}C]-formic acid—corresponding to $F = 0 \leftrightarrow 1$—splits into two lines ($F = 0$, $n = 2$) in the bias field. Spectra of ^{13}C-methanol ($^{13}CH_3OH$) display similar patterns: in zero field, the $^{13}CH_3$ group gives rise to two observable transitions, one at $^1J_{CH} \approx 140$ Hz ($F = 0$ to $F = 1$) and one at $2 \times {}^1J_{CH} \approx 280$ Hz ($F = 1$ to $F = 2$). The perturbing field splits these into a doublet ($F = 0$, $n = 2$) and a sextet ($F = 1$, $n = 6$), respectively. These patterns reveal the quantum numbers involved in each transition, so they may be used to assist assignment and fitting of complicated spectra or lift ambiguity about the chemical structure of the sample.

At higher fields up to around 10^{-4} T, the strength of the Zeeman interaction becomes comparable to the J-couplings and the complexity of the NMR spectrum for coupled heteronuclear spins can rapidly increase. The NMR spectra at these fields often contain an even larger number of resonances for a number of distinct spin-spin couplings. The form of such spectra has been studied theoretically and experimentally measured using both SQUID and vapor cell magnetometers.[62–66] As an example, ^{13}C methanol in a field of 5×10^{-6} T yields a spectrum that contains approximately 10 observable transitions in the frequency range 0-400 Hz, yet the molecule has only one distinct J_{CH} coupling.[66]

III. HARDWARE

A. Magnetic shielding

A magnetic field of $\sim 10^{-10}$ T—below which we accept is a "zero field" for liquid-state samples in the experiments concerned—is established by multiple concentric layers of magnetic shielding as illustrated in Fig. 2(a). Depending on the configuration and size of both the magnetometer and the NMR sample, 3 to 5 layers of mu-metal shielding are used on the exterior. The photograph in Fig. 2(b) shows an example of commercial shields (model MS-1F, Twinleaf LLC) and home-built interior components. The layers of mu-metal collectively attenuate the ambient magnetic field (e.g., of the earth) so the enclosed region is shielded by a factor 10^5-10^6.[35,67] At this level of shielding, ^{1}H Larmor frequencies are below 10^{-3} Hz. An innermost shield made of ferrite is used to minimize Johnson noise from the mu metal layers. Inside the shield there is a set of coils in order to produce fields oriented along the y (solenoid coil, 1.5×10^{-4} T/A), x, and z axes (saddle coils, 8.0×10^{-5} T/A) to cancel any remaining field around the cell or supply bias fields up to around 10^{-6} T. The coils are a set of copper traces printed on Kapton, rolled into a cylinder. Current is supplied to the coils from low noise, precision sources (Krohn-Hite model 523). The internal cylindrical volume measures approximately 150 mm in length and 100 mm in diameter.

Care should be taken to exclude objects with permanent magnetization from proximity to the mu-metal and ferrite layers. The shielding performance of both materials is degraded when magnetization is acquired, and in the worst case, the shield may become magnetically saturated. Weak magnetization of the shields can be removed by using the following degaussing method: A thick, insulated wire (American gauge 20 or thicker) rated up to at least 10 A is looped through the shield as many times as possible, 20-30 turns normally being sufficient. This wire is connected in series with two Variacs and the mains power supply (110 V, 60 Hz). By adjusting the Variac outputs in an alternating fashion—changing one by a small amount, then the other, and so on—the current is increased to approximately 10 A and then returned slowly to zero. One up-down cycle typically takes 5-10 min. The step size in the degaussing current that results from adjusting a Variac is fairly large by adiabatic demagnetization standards.[68] However, residual magnetization of the shield is small enough for our purposes, provided at low current the fields are reduced slowly.

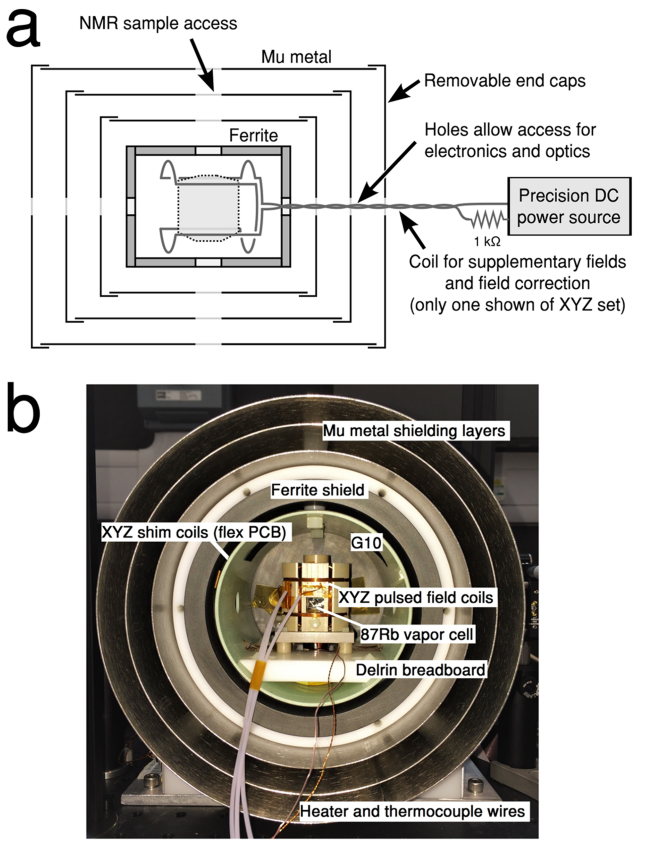

FIG. 2. Apparatus for generating the zero/ultralow magnetic field. In (a), three layers of mu metal attenuate the ambient field of the enclosed volume down to a level of 0.1 nT. Currents on the order of milliamps to microamps can be applied through a set of coils to produce fields along the x, y, or z axis between 0.1 and 1000 nT within the dotted/shaded region. The photograph in (b) shows an example of a commercially available shield set (Twinleaf LLC, model MS-1F, 8-in. diameter outer shield), viewed from one of the ends after removal of the end caps.

The magnetic shields also contain additional access holes of approximately 15 mm diameter to allow entrance of the pump/probe laser beams, the NMR sample, and electrical wiring required for the field coils and the vapor cell heater (see Sec. III D). These holes do not appear to significantly affect the shielding quality in the central working region.

B. Polarization

1. *Ex situ: Zeeman polarization*

The NMR experiment must begin with polarized nuclear spins, i.e., populations of the nuclear spin states must not be

equal. The most general way to initialize spin polarization is to couple the nuclei to a magnetic field ($\boldsymbol{B}_{\rm pol}$, via the Zeeman interaction) and allow the populations of the spin eigenstates to reach thermal equilibrium. For field strengths 10^{-3} T$< |B_{\rm pol}| < 10^{2}$ T and temperatures $T > 1$ K, the thermal polarization of a single spin-1/2 can be approximated by

$$p = \gamma |\boldsymbol{B}_{\rm pol}| / 4\pi k_B T, \tag{4}$$

where $k_B = 2.084 \times 10^{10}$ Hz K^{-1} is Boltzmann's constant and the orientation is parallel to $\boldsymbol{B}_{\rm pol}$. The normalized spin-1/2 density operator under these conditions is given by $\rho_{\rm eq} \approx (1/2 + p\boldsymbol{I} \cdot \boldsymbol{B}_{\rm pol}/|\boldsymbol{B}_{\rm pol}|)$ (tr$(\rho) = 1$). Thus, ^{1}H nuclei at room temperature in a field of 2 T will acquire an equilibrium polarization of around 7 ppm. This leaves considerable room for improvement since, by definition, the polarization can be as large as $|p| = 1$. Nevertheless, for many of the basic experiments described in this paper, the method is sufficient. The level of polarization is also highly consistent, as long as time is left for the thermal equilibrium to be reached, thus suitable for multi-dimensional NMR and experiments involving phase cycles or other types of signal addition.

As explained earlier, strong magnetic fields (above 10^{-1} T) should not be applied within the magnetic shields, so the procedure for polarizing the nuclear spins requires an *ex situ* approach, unless a hyperpolarization scheme is used that works at ultralow field, as exemplified in Sec. III B 2. The sample is polarized in a magnet located a safe distance away from the shields and is then shuttled inside. In our setup, a 2 T Halbach array magnet is placed on a shelf above the shields at a distance of 10-20 cm. The sample is placed in a standard 5 mm outer diameter (o.d.) NMR tube and is shuttled between the magnet and the center of the shield inside a fiberglass tube whose inner diameter (i.d.) is slightly larger than 5 mm and whose o.d. easily fits through the holes in the shielding material. This arrangement is illustrated in Fig. 3(a). The sample can be raised for subsequent re-polarization by applying suction to the top of the tube. Regulation of air pressure at the top and base of the fiberglass tube controls rates of ascent and descent. Fluidic transport may be used as an alternative: two containers may be positioned at fixed locations in the permanent magnet next to the vapor cell magnetometer and the liquid sample pumped between these.[28,31] Other setups may be engineered but have not been tested.

The time scale of the shuttling operation, specifically the speed of switching between different field regimes, is an important consideration in a ZULF NMR experiment. The sample should be shuttled much faster than the relaxation time of the spins so as to preserve as much of the initial polarization as possible. This can be problematic for molecules containing nuclei with nonzero quadrupole moments (including ^{2}H, ^{14}N, and all halogens except fluorine) since scalar relaxation of the second kind[4] is a significant mechanism at low field causing near-complete loss of the spin polarization within a few tens of milliseconds. A second consideration is the change in direction and magnitude of background magnetic fields, including the fringe field of the polarizing magnet and the field due to the earth. The transport can be performed adiabatically (slow relative to the spin dynamics) or suddenly (fast relative to spin

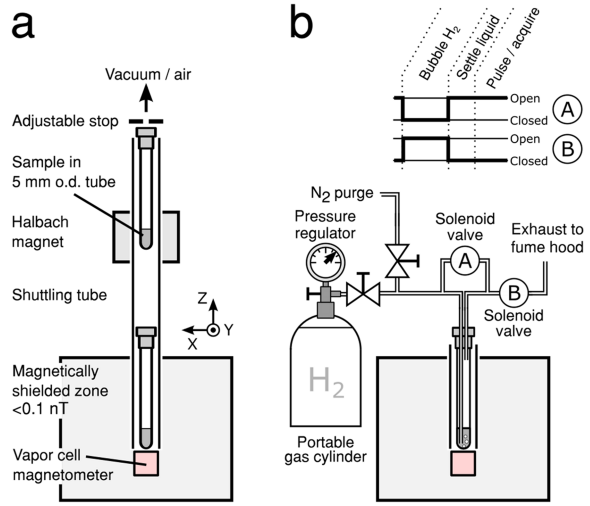

FIG. 3. Schemes for nuclear spin polarization of a substrate prior to a ZULF NMR experiment: (a) thermal prepolarization in a permanent magnet, followed by shuttling; (b) polarization via interaction with parahydrogen.

dynamics). The difference is that an adiabatic transfer produces polarization in the ZULF eigenstates of the spin system, whereas a sudden transfer leaves the initial density matrix unaffected and may lead to detectable coherences as soon as the sample arrives in the ZULF detection region.

These differences can be seen in how the density operator is influenced by the rate at which the sample is transported through the various magnetic field gradients. If the rate of angular change in the effective magnetic field (given by $d\alpha/dt$) is similar to the nuclear precession and/or the spin-spin coupling frequencies (ν), then ill-controlled spin dynamics can result. Therefore, the transport either has to be much faster (nonadiabatic, $d\alpha/dt \gg |\nu|$) or much slower (nonadiabatic, $d\alpha/dt \ll |\nu|$) than the spin dynamics.

If the transit between the polarizing field and ZULF is rapid, the high-field thermal polarization is "instantly" brought into the ZULF and ignoring relaxation is essentially unchanged. For our example of [^{13}C]-formic acid, the density operator would be approximately

$$\rho = (1/2 + p_H I_z^{\rm H} + p_C I_z^{\rm C})/2, \tag{5}$$

where the polarizations are $p_H = (\gamma_H B/4\pi)/(k_B T)$ and $p_C = (\gamma_C B/4\pi)/(k_B T)$. Even for this simple system, $\rho(0)$ does not commute with the zero-field spin Hamiltonian (the operator for scalar coupling, $\boldsymbol{I}^{\rm H} \cdot \boldsymbol{I}^{\rm C}$) due to the component $(I_z^{\rm H} - I_z^{\rm C})$ and therefore sudden switching generates spin coherences between the ZULF eigenstates that result in a time-dependent magnetization. Sudden switching is achievable by rapid sample shuttling, typically where transport is completed within a time of 10–20 ms over a displacement of 20-30 cm.[69] Alternatively, the sample can be slowly shuttled in a "guide field" along the shuttling path of strength on the order of 10^{-5}-10^{-4} T, produced by a solenoid coil wound along the length of the shuttling tube. The field maintains a Zeeman eigenbasis until the sample is stationary next to the magnetometer, inside the shields. At this point, the solenoid field is rapidly quenched (<10 ms) to convert suddenly between the Zeeman (high field) and ZULF eigenbases.

At the other extreme, if the sample is shuttled slowly into the low field the transport is adiabatic. It is desirable to transport the polarized spins adiabatically through the fringe fields (meaning the field orientation changes slowly relative to the speed of nuclear precession) such that the spins remain oriented along the axis of the total magnetic field, which is not necessarily parallel to $\boldsymbol{B}_{\mathrm{pol}}$. The populations of the high-field eigenstates are then smoothly transferred to the ZULF eigenstates, resulting in a new density operator,[18]

$$\rho \rightarrow \left(1/2 + \frac{p_H + p_C}{2}(I_z^{\mathrm{H}} + I_z^{\mathrm{C}}) - (p_H - p_C)[\boldsymbol{I}\cdot\boldsymbol{S} - I_z S_z]\right)/2. \quad (6)$$

The adiabatic method does not immediately produce an NMR signal at zero field because the density matrix operator commutes with the spin Hamiltonian. Subsequent manipulations, such as pulsed fields, are required. These are described in Sec. III C.

2. In situ: Parahydrogen-induced polarization (PHIP)

A different method of polarizing the sample is to expose it to para-enriched dihydrogen (H_2), which contains up to unity polarization in the nuclear singlet state of the proton pair. Polarization from H_2 may be transferred to the target molecule via spin-spin couplings. This strategy is frequently used to increase the signal strength in high-field NMR/magnetic resonance imaging (MRI) since the enhancement can be several orders of magnitude beyond the Zeeman polarization obtained by magnets.

There are numerous ways to create these couplings. One is a hydrogenation reaction, such as addition of polarized H_2 molecules at double or triple bonds in the target molecule.[70,71] A non-hydrogenative way involves reversible complexation at a metal ion, where both H_2 and the substrate bind as ligands and spin coupling arises due to the presence of a common set of molecular orbitals.[72] Usually, a reversible reaction is desired, in order to polarize the spins without altering the chemical properties or structure of the analyte. In both types of reaction, PHIP enhancements depend strongly on the physical conditions, the chemical nature of the analyte, the kinetics of the spin order transfer, and the relaxation times. For molecules incorporating ^{15}N or ^{31}P lone pairs,[73] the non-hydrogenative route is efficient in the regime of 1 to 10 μT where the J couplings to parahydrogen are similar in magnitude to the Zeeman interaction, leading directly to the polarization of the heteronuclei.[74,75]

The appeal of parahydrogen induced zero-field NMR experiments is that sample shuttling is avoided establishing "NMR without magnets" as it was coined in the popular press. A scheme is shown in Fig. 3. The substrate and catalyst are dissolved in solution and contained in a 5 mm o.d. NMR tube. Para-enriched H_2 is bubbled into this solution through a 1/32 inch o.d. Teflon tube, where the flow is controlled by the two solenoid valves "A" (normally open) and "B" (normally closed) triggered by the data acquisition system. Hydrogen is bubbled for a timed interval, during which the reaction occurs, then the liquid is allowed to settle for 100 ms before finally the NMR experiment is started.

With these methods, ^{13}C NMR signals can be detected at the low natural abundance of ^{13}C (1.1%)[76,77] and also ^{15}N spectra can be obtained at the even lower natural abundance of 0.36%,[78] enabling the application of ZULF NMR to the spectroscopy of organic molecules. Detection of the NMR signals in the ZULF may play a central role in understanding the details of the hyperpolarization mechanism in low fields because hyperpolarization is detected directly at the location where it is created.

C. Encoding

1. Pulsed field excitation

For NMR pulse sequences, we use three orthogonal sets of Helmholtz coils (28 AWG enameled Cu wire, 3 cm diameter, 6 turns, 230 μT/A, 1.0 Ω) inside the shields, as shown in Fig. 4(a). The coils are wound on grooves that are machined in a polyether-ether-ketone (PEEK) block and are positioned such that the fields generated are centered on the sample when just above the magnetometer and are oriented along the laboratory x, y (horizontal) and z (vertical) directions as indicated. To apply pulses, the desired waveform is written as a list of time/voltage coordinates (t, V_x, V_y, V_z) in a file on a computer. A microcontroller and digital-analog converter (e.g., National Instruments USB 6229) converts these data into a three-channel analog output voltage (16-bit, −5 V to +5 V). Each output channel is fed into a low-distortion controlled-current amplifier (AE Techron LVC2016, maximum output 10 A at 1.0 Ω load), whose output is connected to one of the coils. It is important to minimize current noise in the pulse coils since these surround the alkali vapor cell and can significantly add to the magnetic field noise of the magnetometer when a closed loop is formed. This is achieved by switching between closed/open loop coils with bipolar field-effect transistors [15 V switching voltage, lower-right part of Fig. 4(a)]. A high logic voltage is applied to the closed coil circuit before applying pulsed fields, while a low logic voltage opens the circuit to minimize noise during detection periods. An optocoupler is preferential to electrically separate the low-power (logic) and high-power sides of the pulsing circuit, in particular to protect the logic circuit from high voltage spikes that might occur during rapid switching the inductive load as well as preventing the formation of ground loops in the testing equipment. High-voltage field-effect transistors (FETs) and bipolar-junction transistors should be used to withstand the voltage spikes and enable current switching and settling times below 5 μs.

In many NMR experiments, it is necessary to perform spin-selective reorientations and the ZULF is no exception. Constant-amplitude direct-current pulse waveforms can suffice for this job as follows. If we ignore the effects of spin-spin couplings, each spin precesses about the net field $\boldsymbol{B}_{\mathrm{pulse}}$ with an angular velocity $\gamma_i \boldsymbol{B}_{\mathrm{pulse}}$ that depends on the gyromagnetic ratio, thus allowing a change in relative orientation. Ignoring the spin coupling terms is a good approximation provided that the pulses satisfy $\tau_{\mathrm{pulse}}|J| \ll 1$ and $|\gamma B|/2\pi \gg |J|$, which is usually the case for $|\boldsymbol{B}| > 100$ μT and pulse flip angles on the order of a few radians.

In [^{13}C]-formic acid, a DC field along the x axis $\boldsymbol{B}_{\mathrm{pulse}} = \{B_x, 0, 0\}$ for a duration $\tau_{\mathrm{pulse}} = 4\pi/|\gamma_{\mathrm{H}} B_x|$ would result in rotations of ^{1}H and ^{13}C spin polarization about x through

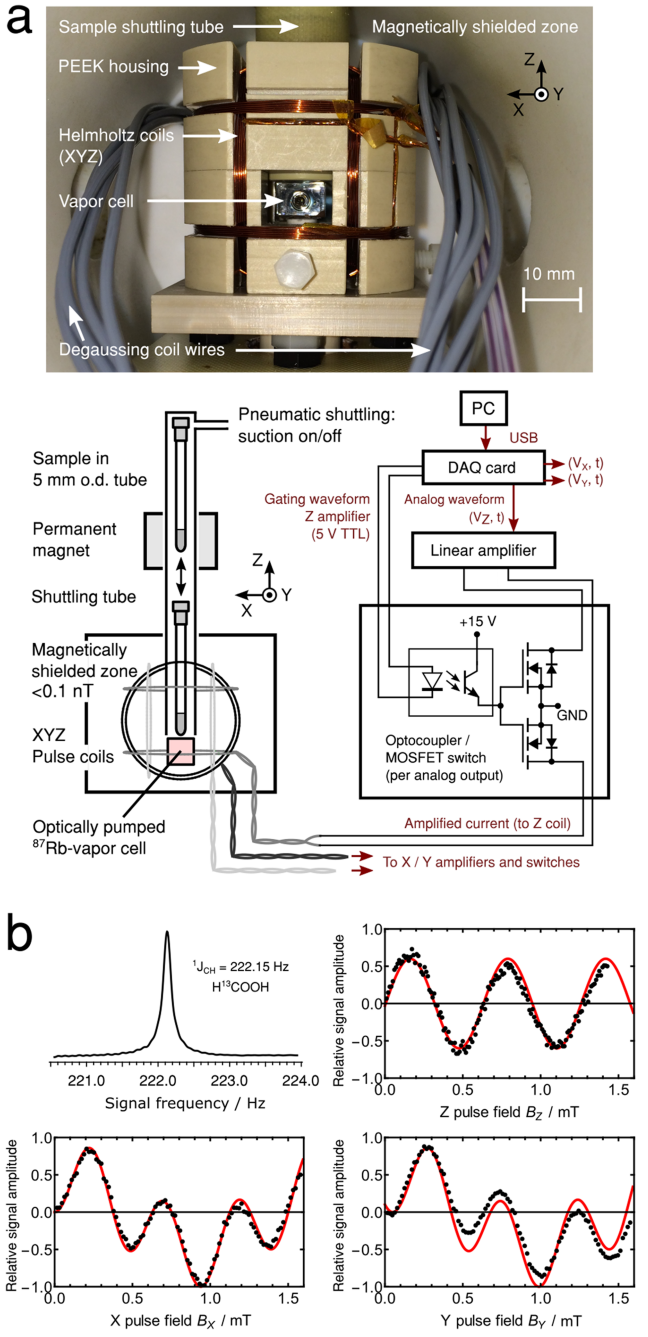

FIG. 4. Illustration of the pulsing coil setup in the ZULF NMR spectrometer: (a) photograph and schematic showing the arrangement of the coils around the vapor cell and control interface; (b) zero-field NMR signal amplitude of [^{13}C]-formic acid versus amplitude of a DC excitation pulse, following prepolarization and adiabatic shuttling into zero field. Pulses were applied via the x, y, or z axis coils, with a duration a 50 μs.

angles 4π and $4\pi|\gamma_C/\gamma_H| \approx \pi$, respectively. This pulse allows an observable signal to be excited from the postcursor state after adiabatic shuttling, given in Eq. (6). We can see that a 180-degree rotation of either spin species converts $(I_z^H + I_z^C)$ into $\pm(I_z^H - I_z^C)$, which as explained in the Introduction is nonstationary under the zero-field Hamiltonian.

Figure 4(b) shows the amplitude of the zero-field NMR signal for [^{13}C]-formic acid after a 50 μs pulse versus the pulse-field amplitude along the x, y, and z coil axes. The change in spin orientation changes the coefficient of the spin order $(I_z^H - I_z^C)$ and thus the signal with pulse length τ_{pulse} as $\sin[(\gamma_H + \gamma_C)B_x\tau_{pulse}/2]\sin[(\gamma_H - \gamma_C)B_x\tau_{pulse}/2]$ which is plotted as the solid curve. The signal after x- and y-field amplitudes is ideally the same since the amplitude of $(I_z^H - I_z^C)$ that results from each rotation does not depend on the direction of the field in the xy plane.

The dependence on field amplitude B_z along the z axis follows the function $\sin((\gamma_H - \gamma_C)B_z\tau_{pulse})$, which is different because it is the product term $\boldsymbol{I}^H \cdot \boldsymbol{I}^C$ [cf. Eq. (6)] that generates the observable rather than the orientation parallel to z. Overall, these curves provide an accurate calibration of the magnetic field vs applied current to the coils, which is needed in order to implement sequences of many pulses where precise nuclear spin reorientation is demanded, including spin-echo pulse trains[79] and spin decoupling.[80,81] Pulse trains also offer the option to measure the zero-frequency component of the NMR signal by "lock-in detection": the nuclear magnetization is periodically inverted using 180° pulses to produce a signal looking like a square wave, which is then separable from DC background signals.[53]

The pulsing setup outlined in Fig. 4(a) allows the amplitude of applied fields to be varied smoothly, enabling one to implement conventional "high-field" NMR methodology in which resonant AC fields at the Larmor frequency are used to obtain spin species selectivity: A DC pulse ($|\boldsymbol{B}_{pulse}| < 2$ mT, for several seconds without noticeable heating effects) is applied along one axis, and at the same time, a much weaker AC pulse ($|\boldsymbol{B}_{pulse}|_{max} < 0.02$ mT) is applied with the Larmor frequency of the selected spins, up to several tens of kHz.[82] A larger number of coil windings would allow DC fields of several tens of milliteslas to be reached, where chemical shifts are large enough to be resolved and exploited. For example at 10 mT, a 100 ppm chemical shift of ^{13}C corresponds to a frequency difference of 10 Hz.

2. *Extremely-low-frequency pulses*

Strong DC pulses of the type described above and illustrated in Fig. 4 are broadband with respect to the zero-field spectrum. The reason for this is that the Larmor precession frequencies of the sample spins in the applied fields are much greater than the eigenfrequencies of the intramolecular Hamiltonian ($|(\gamma_j \pm \gamma_k)\boldsymbol{B}_{pulse}| \gg |2\pi J_{jk}|$) that is the source of the ultralow-field signal. Therefore, such pulses affect all spins in the spectrum.

If one wishes to exert control over individual transitions, one should use low-amplitude modulated pulsed fields that are much weaker than the internal Hamiltonian and resonant with a transition of choice.[83] It can be shown that under these conditions, the spin order is driven selectively between spin eigenstates connected by the resonant field. The rate of these transitions is calculable given the total and projection angular momentum quantum numbers of the states involved and the strength of the resonant field.

D. Detection

1. *Principles of optical magnetometry*

To probe the spin dynamics, we detect the magnetic field emanating from the NMR sample with an atomic

magnetometer. We exploit an effect known as *magneto-optical rotation*. This effect involves the passage of linearly polarized light through a medium and the subsequent rotation of its polarization plane due to the difference in refractive indices $n_\pm$ for the two circularly polarized components ($\sigma^\pm$) of the light. For a path length l and light frequency ν, the rotation angle is given by

$$\varphi = (n_+ - n_-)\pi\nu l/c. \tag{7}$$

If the difference in refractive indices $(n_+ - n_-)$ depends on the magnetic field at the material, the circular birefringence allows the magnetic field to be determined. The first examples of such effects to measure nuclear magnetization date back over 50 years.[84–87] Below, we present only a brief account of the effect used in our apparatus. More general reviews of magneto-optical effects can be found in the literature.[34,88–90]

In our case, the atomic vapor of an alkali metal is probed near the D1 atomic resonance ($^2S_{1/2}$ to $^2P_{1/2}$ transition), and the refractive index is bestowed by absorption of light, characterized with a sharp frequency dependence near resonance. We may consider the D1 transition without hyperfine effects and so assume a four-level system comprising the excited-state ($^2P_{1/2}$) and ground-state ($^2S_{1/2}$) doublets, each with projections of the atomic spin $m_J = -1/2$ and $m_J = +1/2$. Light that is circularly polarized along the quantization axis may induce transitions $\Delta m_J = \pm 1$, where the sign indicates interaction with σ^+ or σ^- light.

A difference $(n_+ - n_-)$ may be encoded with a longitudinal magnetic field B parallel to the light beam because the absorption maxima of the two transitions $\Delta m_J = \pm 1$ shift in opposite directions, $\nu_0^\pm = \nu_0 \pm g\mu_B B$. Here g is the gyromagnetic ratio of the atom (the ground state Landé factor) and μ_B is the Bohr magneton. The dependence of the real refractive indices $n_\pm$ on B is related to the imaginary part of the (Voigt) absorption line shape, $\mathcal{V}(\nu - \nu_0^\pm)$, via the Kramers-Kronig relations. Taking into account the populations $\rho_\pm$ for the ground states $m_J = \pm 1/2$, the difference can be expressed as

$$\begin{aligned}(n_+ - n_-) \propto\ & \rho_-\mathrm{Im}[\mathcal{V}(\nu - g\mu_B B - \nu_0)] \\ & - \rho_+\mathrm{Im}[\mathcal{V}(\nu + g\mu_B B - \nu_0)],\end{aligned} \tag{8}$$

so at any frequency ν within the resonance line, the refractive indices are unequal. This phenomenon for the case of resonant absorption in atomic vapors is named the Macaluso-Corbino effect.[91–93]

Our magnetometer involves a strongly amplified version of the Macaluso-Corbino effect, which exploits nonlinear optical properties of the alkali atom vapor. As well as shift the frequencies of the $\Delta m_J = \pm 1$ transitions, the absorption coefficients are strongly debalanced by optical pumping. The optical pumping stems from the interaction of the atoms with circularly polarized light, which induces redistribution of atomic population among the Zeeman sublevels. As the sublevels correspond to specific projections of spin onto the quantization axis, this leads to spin polarization of the medium. The resulting magneto-optical effect is summarized in Fig. 5 and explained below.[94,95]

If the pump light is circularly polarized and propagates along the y axis (unit vector $\boldsymbol{e_y}$) of the instrument, the atomic polarization $\boldsymbol{S}$, determining the optical anisotropy, is determined by the Bloch equation

$$d\boldsymbol{S}/dt = [g(\mu_B/\hbar)\boldsymbol{B} \times \boldsymbol{S} + R_{\mathrm{OP}}(\boldsymbol{e_y}/2 - \boldsymbol{S}) - R_{\mathrm{rel}}\boldsymbol{S}]/q, \tag{9}$$

where q denotes the nuclear slowing-down factor, R_{OP} is the rate of optical polarization, and R_{rel} is the rate of polarization decay in the ground state.[35] For the case of zero field, $\boldsymbol{B} = \boldsymbol{0}$, a steady-state atomic polarization ($\mathrm{d}\boldsymbol{S}/\mathrm{d}t = \boldsymbol{0}$) is given by $\langle S_y\rangle = S_0 = (+1/2)R_{\mathrm{OP}}/(R_{\mathrm{OP}} + R_{\mathrm{rel}})$ and $\langle S_x\rangle = \langle S_z\rangle = 0$ [Fig. 5(a)].

For a nonzero value of $\boldsymbol{B}$, atomic spin precession causes a component of the steady-state polarization that is perpendicular to both $\boldsymbol{B}$ and the pump beam axis. For a field $\boldsymbol{B} = \boldsymbol{e_z}B_z$, the steady-state solution of Eq. (9) yields a finite component $\langle S_x\rangle = S_0(g\mu_B/\hbar)B_z$, such as that illustrated in Fig. 5(b).

To probe the polarization component $\langle S_x\rangle$, the linearly polarized probe beam is aligned with the x axis [Fig. 5(c)].

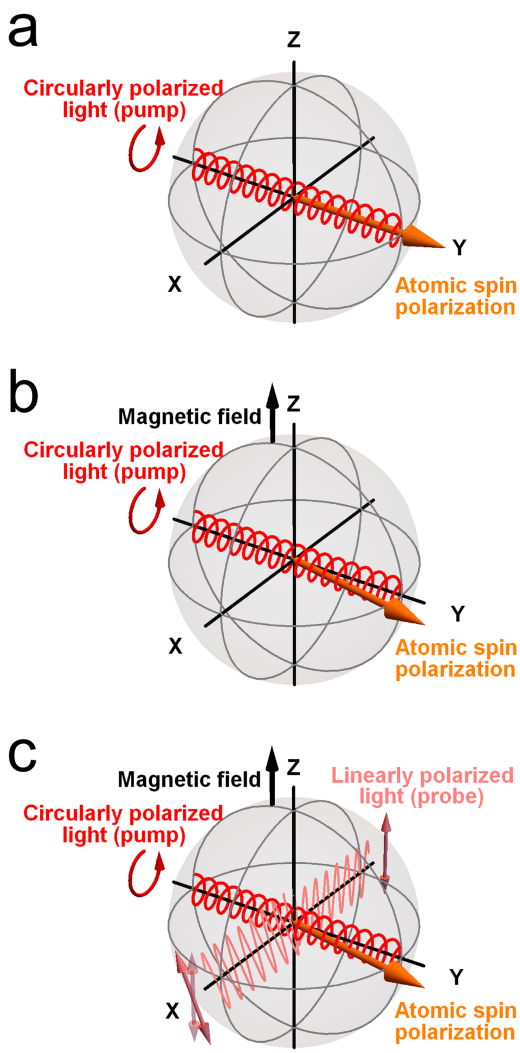

FIG. 5. Scheme for optical pump-probe magnetometry. The orange-colored arrow represents the average spin polarization $\langle S\rangle$ of alkali atoms in the magnetometer: (a) incident circularly polarized pump light induces polarization along the y axis; (b) an off-axis component of steady-state polarization arises in a finite magnetic field B_z due to spin precession: $\langle S_x\rangle \propto B_z$. In (c), the plane-polarized probe light beam passes through the vapor along the x axis. The plane of polarization is rotated by an angle $\varphi \propto \langle S_x\rangle$, allowing B_z to be measured.

The component $\langle S_x \rangle$ corresponds to a ground-state population difference across the $m_J = \pm 1/2$ ground states. In such a configuration, the polarization of the probe is a direct measure of the magnetic field. The rotation is enhanced by many orders of magnitude compared with the linear Macaluso-Corbino effect. It is hence called nonlinear magneto-optical rotation.

In general, Eq. (9) can be solved to give the rotation angle φ as a function of the magnetic field in any direction. The probe beam polarization, giving the magnetometer signal, is sensitive to fields along all axes x, y, and z according to the function

$$\varphi \propto S_x = S_0 \frac{(\Delta B)B_z + B_x B_y}{\Delta B^2 + B_x^2 + B_y^2 + B_z^2}, \tag{10}$$

which is a dispersive Lorentzian with a linewidth $\Delta B = (g\mu_0/\hbar)/(R_{\mathrm{op}} + R_{\mathrm{rel}})$ when $B_y = B_x = 0$.[35] However, the magnetometer is most sensitive to B_z when operated in the region $|B_y| \ll \Delta B, |B_x| \ll \Delta B$, where the slope $\mathrm{d}\varphi/\mathrm{d}B_z$ is largest ($S_x \approx S_0 B_z/\Delta B$). The magnetic field generated by an NMR sample is generally not larger than 1 pT. This lies well within the central part of the dispersion curve ($|B_z| \ll |\Delta B|$) resulting in a magneto-optical rotation where the angle φ is linearly proportional to the NMR signal. This justifies our choice of the observable in Sec. II.

The magneto-optical effect in this regime can be characterized by a Verdet coefficient (V), defined as the rotation angle φ at a given wavelength per unit path length l and applied field B_z: $\varphi = VB_z l$. For Faraday rotation in most solid and liquid materials, V does not usually exceed 1000 (rad/T·m). For sparse, optically pumped alkali vapors in the SERF regime, the Verdet coefficient can be as large as 10^{12} (rad/T·m). Therefore, on a per-atom basis, the atomic magnetometer is more sensitive by around 11-12 orders of magnitude. The fundamental sensitivity of the atomic magnetometer is limited by the ability to determine the atomic spin projection due to the Heisenberg uncertainty principle.[34] For a measurement time T, the uncertainty in B is given by the expression

$$\delta B \sim \frac{h}{2\pi g \mu_B} \sqrt{\frac{R_{\mathrm{rel}}}{NT}}, \tag{11}$$

where N is the number of atoms involved. In the literature, δB is frequently given per unit bandwidth in units of T/Hz$^{1/2}$. Typically, although not universally, a bandwidth of 1 Hz corresponds to a measurement time of $T = 0.5$ s.

Although Eq. (11) implies that large numbers of alkali atoms are favored, there are some caveats. A dense atomic vapor incurs a high rate of atom-atom spin-exchange collisions. This corresponds to an increase in R_{rel}. As the two hyperfine ground states of alkali atoms are characterized with nearly opposite Landé factors (they precess in opposite directions in a magnetic field), the spin-exchange-induced transitions between the hyperfine states introduces a relaxation that for a broad range of temperatures (70-170 °C) prevents from increasing the magnetometric sensitivity. However, this changes even at higher temperatures and vapor densities. The SERF regime at ultralow fields is characterized by a slow precession of the atomic spins relative to the rate of atom-atom collisions. Here the hyperfine state is rapidly (and randomly) switched and averaged, such that spin-exchange collisions no longer act as a significant relaxation mechanism.[37,38] Relaxation in the SERF regime is consequently dominated by spin-destruction collisions, where the cross section is between 2 and 4 orders of magnitude smaller than for spin exchange in alkali vapors,[96,97] allowing sensitivities that approach close to the spin-projection limit below 1 fT/Hz$^{1/2}$.[20,27,28,30,39,40]

Since the NMR signals of interest correspond to time-dependent fields, an important parameter is magnetometer bandwidth. The response of the magnetometer to a change in the magnitude of B_z occurs with the time constant $1/T_2 = (R_{\mathrm{op}} + R_{\mathrm{rel}}/q)$ of the alkali atom spins, thus the response to the oscillating field versus frequency is a Lorentzian profile with half width $1/(2\pi T_2)$ at half maximum (i.e., Fourier transform of the response curve).[35] We see that an increased magnetometer bandwidth then comes at the expense of a reduction in sensitivity, since the two quantities scale oppositely in T_2. For our instrument, an acceptable sensitivity is 20-30 fT/Hz$^{1/2}$, which we find is achievable over the 0-500 Hz frequency range.

Finally, we comment that for our setup, the pump and probe beams are at 90° to one another, however, other optical configurations can in principle be used. For example, a single laser beam can be used for simultaneous pumping and probing or parallel pump and probe beams.[50] In some of these arrangements, the magneto-optical effect is detected through absorption of light by atoms rather than the rotation of the probe light polarization plane. To our knowledge, while these methods are equally straightforward to implement, they have so far not been used in the detection of ZULF NMR.

2. Magnetometer setup

In our setup, rubidium-87 is used as the atomic medium and is confined to a cuboidal cell made from borosilicate glass, inner dimensions measuring 5×5×8 mm^3 [2-5 mg ^{87}Rb of isotopic purity 98%, N_2 buffer gas at 700 Torr = 93 kPa, Twinleaf LLC, see the top-left part of Fig. 6(a)]. This cell is uncoated on its walls and is heated to temperatures of 170-190 °C to achieve a high vapor density of alkali atoms in the SERF regime. The nitrogen acts to improve optical pumping of the alkali atoms as a non-radiative relaxation source and as a buffer gas to minimize relaxation due to collisions with the cell walls.[98]

The operating temperature of the Rb cell is reached by resistive-inductive heating through a 5-meter length of double-twisted 27-gauge enameled copper wire (of resistance around 2 Ω), which is wrapped approximately 50 turns around a thermally conductive cylindrical spool made from aluminum nitride [Shapal Hi-M, Precision Ceramics, room-temperature thermal conductivity 92 W/(m · K)]. The assembly is insulated by placing it inside an alumina tube. As shown in Fig. 6(a), the glass cell is cemented (Omegabond 400) to a separate short (5 mm length) section of the nitride material designed to mate with the top of the spool. The two-part design allows the fragile cell to be easily removed or reattached and kept separate during initial assembly or maintenance/repair of

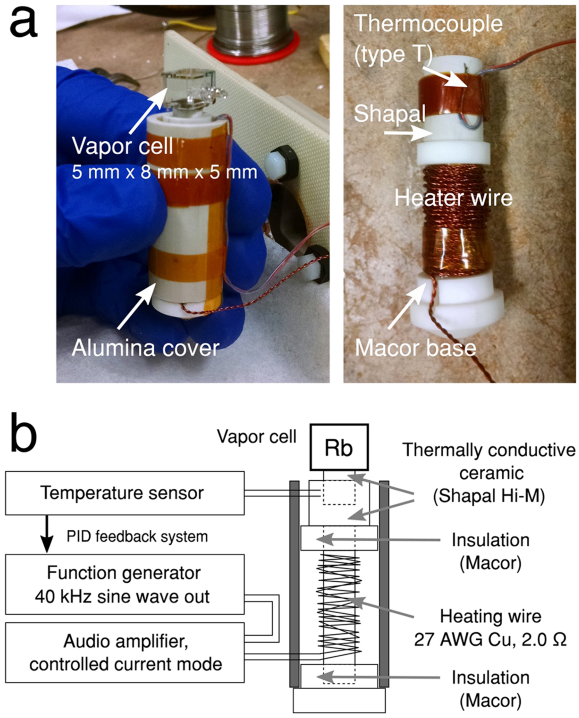

FIG. 6. Details of the heating element and electrical circuit to heat the rubidium vapor cell to its operating temperature.

the heater. The wire is wound as a twisted pair to minimize magnetic fields that could be produced when electrical current is applied.

It is observed that cell heating in the DC mode can present a major source of field noise in magnetometer measurements. Although one can turn off the heater when measurements are made, this is unfavorable since the cell cools down during these times. The preferred mode of heating is continuous AC, using a relatively high frequency (>10 kHz) far away from the signals of interest and outside the sensitive bandwidth [Fig. 6(b)]. A type-T thermocouple is placed near the top of the aluminum nitride pillar, as close to the cell as possible, to measure the temperature, and a proportional-integral-derivative temperature controller (Omega CN9000A model) provides a feedback loop to control the current applied to the heating wire. The supply of alternating current is a low-distortion audio amplifier (AE Techron LVC2016, Crown Macro-Tech series or similar) where the AC input voltage is produced by a function generator and the amplitude is controlled by the feedback. At a 40 kHz heating frequency, a root-mean-square power of approximately 10 W is required to raise the cell temperature to 180 °C.

Thermal insulation of the vapor cell is an important design feature in the experimental setup. While the cell is operated at 170-190 °C to achieve the quoted sensitivities, it is desirable to detect NMR signals from the sample near to room temperature. For insulation, an air or vacuum gap of 0.5-1 mm is left between the vapor cell and the bottom of the shuttling system. The temperature of the air surrounding the NMR sample tube inside the shuttling system may also be regulated. One must minimize temperature gradients across the cell to avoid further broadening of the atomic resonance line and a decrease in the overall sensitivity. The minimization of thermal losses also allows the desired temperature to be reached at lower heating power.

The optical setup is illustrated in Fig. 7. For the optical pumping of the ^{87}Rb vapor, a tunable distributed-feedback (DFB) diode laser is used with a Thorlabs ITC502 laser diode controller. The laser light is tuned to the ^{87}Rb D1 line at a wavelength of 794.970 nm[99] using a wavelength meter/interferometer (e.g., Agilent/HP 86120B, 0.005 nm accuracy). An optical isolator is positioned immediately after the laser collimator to eliminate reflections from the subsequent optical components. This initial beam is plane-polarized, so a half-wave plate is positioned in the path of propagation to allow arbitrary rotation of its plane of polarization. A linear polarizer follows, to allow the light power to be attenuated to the desired level. Transmitted light is then converted to circularly polarized light with a quarter-wave plate whose principal axes are 45° from the axis of the linear polarizer. In normal operation, settings are chosen such that a power of approximately 15 mW arrives at the vapor cell. The typical beam diameter is 5 mm. In addition to the components that

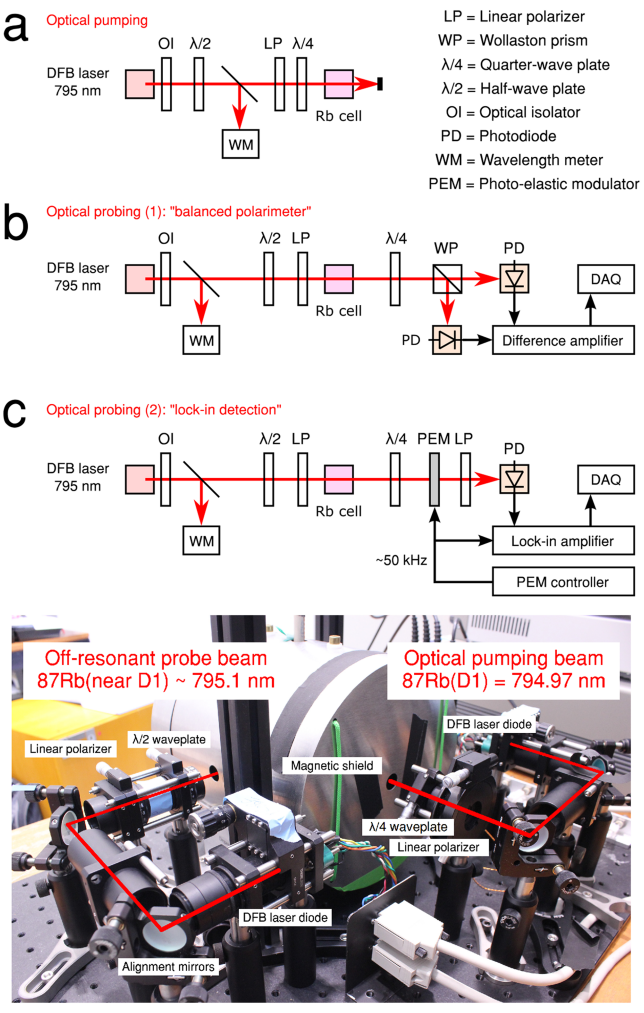

FIG. 7. Layout of optical components used for signal detection: (a) light beam for optically pumping alkali metal spins; optical polarimetry using (b) quadrature or (c) heterodyne photo-detection. The lower photograph illustrates the arrangement of (a) + (b) around the magnetic shield.

control the beam polarization, beam splitters or flip mirrors may be added to divert light into a variety of meters for tuning, locking the laser, or measuring the beam power.

The source of the probe beam is a second DFB laser diode controlled with a separate ITC502 unit and tuned near the D1 line. For the most sensitive detection, one should effect the largest optical rotation on the beam while minimizing resonant excitation of the atoms. The apparatus achieves this condition when the probe laser is detuned between 1 and 2 times the linewidth (in our case, 100–150 GHz) away from the D1 frequency and when the power of the incident beam at the vapor cell is less than 10 mW (beam diameter ~5 mm). Further optimization is described in Sec. III E. Two methods for measuring the optical rotation are outlined in Figs. 7(b) and 7(c). Figure 7(b) illustrates a "balanced polarimeter," where after the alkali vapor imparts rotation, the probe beam is split by a Wollaston prism into perpendicular components of the polarization and the intensities are detected at a pair of photodiodes. These are "balanced" (i.e., zeroed) by adjusting the incident beam's plane of polarization to equalize the detected intensities. The voltage difference between the two photodiodes is amplified (Thorlabs balanced photodiode amplifier, PDB210A 320-1060 nm, gain ~50), so the final output voltage is the response to a change in field and is proportional to the optical rotation angle. It is useful to add a quarter-wave plate in the beam path to correct for additional optical rotation due to birefringent walls of the vapor cell.

The scheme in Fig. 7(c) illustrates a method for heterodyne detection, which aims to minimize the influence of extremely low-frequency noise coming from the apparatus such as $1/f$ noise and laser jitter. The probe beam polarization is modulated at a frequency of around 50 kHz using a photoelastic modulator (PEM, Hinds Instruments model PEM-100). The PEM consists of a birefringent quartz crystal that is stressed by mechanical vibration, induced with a piezoelectric element, along one of its principal axes to retard incident light by up to $\pm\lambda/4$. If the incident light is linearly polarized at 45° to the fast axis of the crystal, the oscillating stress alternates the transmitted light between left and right circular polarizations at the natural resonance frequency of the PEM crystal. This light passes through a linear polarizer, resulting in the intensity becoming modulated at the PEM frequency, which is then detected at a photodiode. Demodulation against the PEM resonance frequency is performed with a lock-in amplifier (Stanford Research Systems model SR830) to give the final output signal. The DC offset in this case can also be zeroed by rotating the quarter-wave plate. The integration time of the lock-in amplifier (10 μs to 100 ms) is chosen as appropriate for the signal-frequency region of interest.

For both detection methods, careful alignment of the pump and probe beams is required both with respect to one another and the sample under study. We find that the pump and the probe should be aligned perpendicular to each other within ~2°. Additionally, detection is most sensitive when the pump and probe beams (i) intersect over a large volume of the vapor cell, ideally its entire volume, and (ii) are as close as possible to the NMR sample.

The output of the differential or lock-in amplifier may be connected to a spectrum analyzer for real-time continuous monitoring of the frequency spectrum and a voltmeter to measure the DC offset voltage. To stabilize the DC offset, a second-order high-pass RC circuit, with a cutoff frequency around 0.3 Hz, is placed immediately after the output of the amplifier.

For NMR experiments, the magnetometer output is recorded digitally using a data acquisition card interfaced with a personal computer (PC) (National Instruments USB 6229, 16-bit ±5 V analog input range). A graphical-user-interface on the PC allows the instrument user to define experimental parameters, including spectral bandwidth, acquisition time, and the number of dwell points, and display the Fourier transform of the recorded data. The program also interfaces the analog and digital input–output (I/O, 5 V logic) needed to operate other parts of the spectrometer, such as setting the waveforms that control the pulse sequences and sample shuttling.

E. Calibrations

When setting up the magnetometer, a number of optimization and calibration procedures should be performed. The field in the vicinity of the vapor cell and the NMR sample must be controlled, in order to (1) operate in the sensitive SERF regime and (2) set known values of the bias fields. The magnetometer signal as a function of frequency must then be measured to determine detection bandwidth. The absolute sensitivity of the magnetometer should also be determined and checked on a regular basis to assess the condition of the vapor cell.

The magnetometer sensitivity is measured by applying an alternating field on the order of 1 pT to 1 nT through one of the x, y, and z field coils. The field is supplied using a function generator connected to the coils in series with a 1 MΩ to 1 kΩ shunt resistor, which produces alternating current in the 1 μA to 1 mA range. The oscillating magnetic field along the corresponding axis around the vapor cell generates a magnetometer response that we call the "test signal."

To observe the test signal, the pump laser beam is tuned near to the D1 transition frequency. Using a power meter, the transmitted power of the probe beam is measured versus frequency. For our vapor cell, we expect and observe a Voigt absorption profile with about 50 GHz (0.1 nm) width as shown in Fig. 8(a). Following this, the probe laser beam is tuned approximately twice the linewidth from the D1 line. The direction of frequency shift is not important although in our case it is on the high-frequency side as this happens to result in a stronger magneto-optical response [Fig. 8(b)]. At the same time, the pump laser is tuned to the center of the optical transition and the power level set to 10 mW. These "crude" settings should allow a test signal amplitude of 1 nT to be detected even at relatively low temperatures of the alkali gas, around 120 °C for ^{87}Rb. To fully optimize the performance of the magnetometer, one should refine the alignment, power, and frequency of both pump (y axis) and probe (x axis) laser beams until the signal-to-noise ratio of the test signal along the z axis is maximized. Sample data for our magnetometer are shown in Figs. 8(b) and 8(c).

The test signal is also used to find the values of the bias currents that cancel remaining magnetic fields. From Eq. (10),

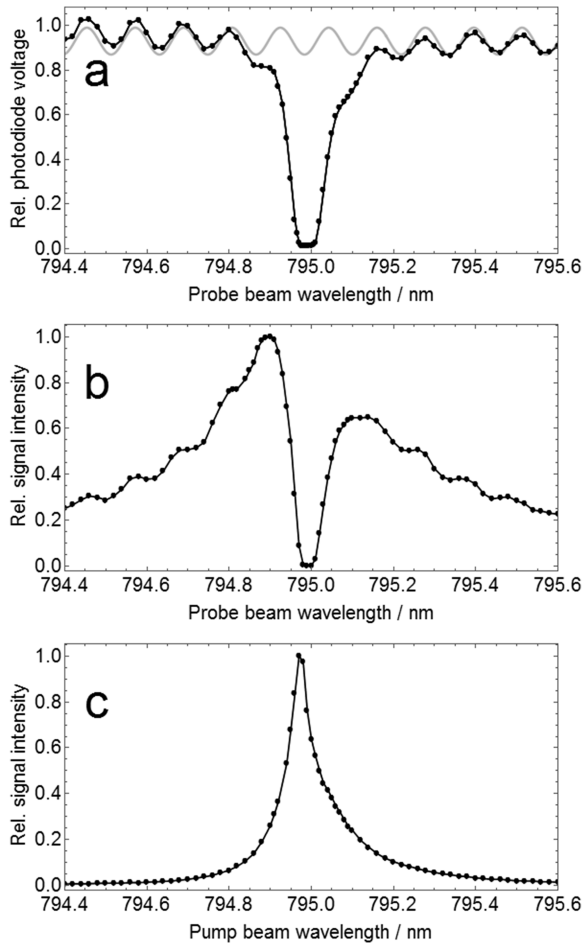

FIG. 8. (a) Optical transmission of 10 mW laser light through the ^{87}Rb vapor cell at 175 °C showing a broad absorbance peak (0.1 nm width at half maximum) at the ^{87}Rb D1 transition. Plots (b) and (c) show, respectively, the magnetometer response to a 20 pT, 100 Hz test signal as a function of pump and probe beam wavelengths. The incident probe beam power is 10 mW, and the power of the optical pumping beam is 20 mW; in (b), the pump beam wavelength is held constant at 794.97 nm, while in (c), the probe beam wavelength is at 794.88 nm. Periodic fringe peaks in (a) and (b), highlighted by the gray curve, are consistent with interference due to a Fabry-Pérot effect at the glass walls of the cell (total thickness ≈ 1.6 mm).

if a slowly oscillating (<100 Hz) test signal is applied in the perpendicular direction to both the pump and probe, the magnetometer response is a dispersive Lorentzian function. The residual B_z is zeroed first. The pump laser beam is blocked from reaching the cell, and the polarization of the probe beam is rotated until the magnetometer response becomes zero. The pump beam is then unblocked and B_z adjusted to zero the DC offset of the magnetometer. To eliminate residual fields B_x or B_y, a ≈5 Hz test signal is applied in turn along the y or x axis, respectively, viewing the magnetometer response on an oscilloscope. A test signal oscillating parallel to the x axis is applied and B_y is adjusted until the response is minimized. The field B_x is then adjusted to minimize the response from a test field oscillating along the y axis. Fields B_x, B_y, and B_z are adjusted iteratively in this way until the test signal is only detected along z. Unfortunately, this protocol does not guarantee a zero field at either the magnetometer or the NMR sample. Finite magnetic fields can arise unintentionally for several reasons: the NMR sample is necessarily located at some distance from the vapor cell, such that gradients in the bias fields can effect a nonzero field at the sample. Also, the test signal does not distinguish B_x, B_y, or B_z from fictitious magnetic fields generated by light shifts or imperfect alignment of the laser beams. For further accuracy, the fields should be minimized by measuring NMR spectra, where the values of the field at the NMR sample are determined from its Larmor frequencies. The field per unit current and the zero bias fields can then be calculated.

We quantify the sensitivity by the smallest test signal amplitude δB_z that is detectable with unit signal-to-noise ratio (SNR) over a 1 Hz measurement bandwidth. The SNR is defined at the peak amplitude divided by the standard deviation of the noise. In our setup, a 100 Hz, 4.4 pT test signal yields an SNR of around 100 when sampled over 0.5 s (=1 Hz bandwidth). The resulting sensitivity is therefore $\delta B_z \approx 30$ fT/Hz$^{1/2}$ at 100 Hz.

The bandwidth of the magnetometer is determined from a set of spectra measured at different frequencies of the test signal. Figure 9 shows the magnetometer signal amplitude and phase relative to a 4.4 pT test signal over the frequency range of 0–400 Hz. The data show that the signal amplitude drops by close to 65 percent, and the phase shift (relative to zero frequency) varies from zero at 0 Hz to almost 3 rad at 400 Hz. These data suggest a usable magnetometer bandwidth of approximately 400 Hz. However, if the noise is dominated by sources from outside the cell instead of the alkali atom spin noise, for example, Johnson noise from the magnetic shield, then the noise is attenuated in the same way and the signal-to-noise ratio does not change strongly across the spectrum,

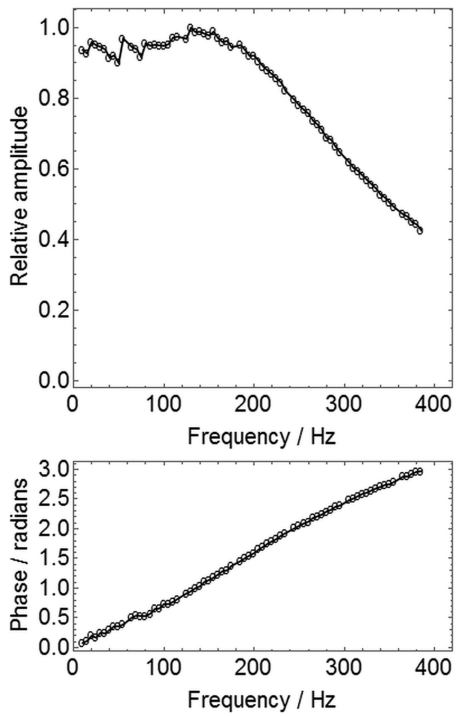

FIG. 9. Plots showing the amplitude and phase of the magnetometer signal in response to a 4 pT sinusoidal test signal, as a function of the test signal frequency.

so the usable frequency range is 2-3 times larger. We find that the SNR of the magnetometer is essentially flat up to 500 Hz, with the exception of vibrationally induced magnetic or optical noise that can degrade sensitivity in the spectral region below 10 Hz. These parameters vary depending on alkali vapor composition, temperature, pump beam power, and other parameters that influence the spin resonance linewidth of the alkali atoms. The shape of the frequency response curve is also strongly affected by the residual fields at a fraction of a mG level that are present on the sensor because in the experiment, we compensate the fields at the location of the NMR sample and not on the SERF sensor.[30] This effect is apparent in Fig. 9 because for a magnetometer at exactly zero field, the maximum of the response curve should occur at zero frequency. In this case, the field gradient between the NMR sample and magnetometer causes the maximum response to shift to approximately 150 Hz. Increased sensitivity over this frequency range due to small field gradients between the cell and the sample can be favorable for J-coupling NMR spectroscopy in the ZULF because it is the range of most one-bond ^{1}H-^{13}C spin-spin scalar couplings.

Although the magnetometer setup is chosen as a compromise between sensitivity and detection bandwidth (inverse of response time), there are some aspects of the NMR experiment that would benefit from a change of conditions. One of these is the time to recover a magnetometer signal following pulsed fields of several mT submitted by the NMR pulse sequences, which increases greatly with alkali vapor temperature and on our setup can be as large as 20-30 ms. In a straightforward pulse-acquire experiment, this dead time of the magnetometer does not cause problems; it is sufficient to omit the data points acquired 30-40 ms after pulsed fields and correct for the time shift via a first-order (frequency-linear) phase correction to the spectrum. However, the response time is generally too long to allow advanced experimental techniques, such as spin decoupling, that involve the so-called "pulse-windowed detection." The aim of such methods is to acquire signal data points during short delays inbetween magnetic field pulses, which may only be a few ms. To reduce the magnetometer dead time without compromising the detection sensitivity, one should be able to rapidly switch the intensity of the pump beam. Following application of pulsed magnetic fields, the intensity should be increased (thereby temporarily increasing R_{OP} and decreasing T_2) to accelerate magnetometer recovery before being returned to the level which allows the NMR signal to be recorded with highest sensitivity. If higher bandwidth is required without compromising the sensitivity, it will be interesting to explore atomic magnetometers employing quantum nondemolition measurements.[100]

Most of our ZULF-NMR experiments are performed with liquid samples whose volume is on the order of 0.05–0.5 mL. The liquids are contained in standard 5 mm or 10 mm o.d. glass NMR tubes. The NMR signal is detected with the tube positioned just above the alkali vapor cell. Since the magnetic field generated by the sample decreases with the third power of distance, flat-bottomed thin-wall NMR tubes are preferred since they reduce the distance between the sample and vapor cell and lead to improved sensitivity. For the 5 mm o.d. tube, the sensitive volume is the lowest 5-10 mm of the liquid corresponding to volumes 100-200 μL. The magnetometer is also suitable for use with microfluidic devices or flow cells,[20,28,49] where the volume of interest is placed as close as possible to the vapor cell.

A preferred sample for calibration and sensitivity determination is neat 99% [1–^{13}C]-formic acid (H^{13}COOH, 26.5 mol/dm^3; zero-field NMR spectrum peak at $^{1}J_{\mathrm{CH}} \approx 220$ Hz). Another choice of the sample is 99% [^{13}C]-methanol (^{13}CH$_3$OH, 24.7 mol/dm^3; zero-field NMR spectral peaks at $^{1}J_{\mathrm{CH}} \approx 140$ Hz and $2 \times {}^{1}J_{\mathrm{CH}}$). Under the quoted conditions, the zero-field NMR signals of these samples are in excess of 100 times the noise floor, corresponding to fields on the order of 1 pT/ml (assuming a ~1 T prepolarization field). For best results, the liquids should be degassed (freeze-pump-thaw) prior to use, in an effort to maximize the natural lifetime of the spin coherences by eliminating dissolved paramagnetic oxygen (O_2).

Finally, the sensitivity of the magnetometer is also strongly dependent on the bias field. This is expected since the relaxation time of the alkali spins depends on the field, particularly when bias fields are strong enough to withdraw SERF behavior (around 100 nT). Additionally there is a dependence because the large difference in the gyromagnetic ratio of the alkali-atom spins and the NMR sample leads to a reduced overlap of the ^{87}Rb resonance with the NMR transition frequencies. This behavior can be seen upon solving Eq. (9) for an oscillating field along the z axis, $\boldsymbol{B} = \boldsymbol{e_z} B_1 \cos(2\pi\nu_1 t)$ in the presence of a bias field $\boldsymbol{e_y} B_y$ along a perpendicular axis. The maximum response is shifted to a non-zero field defined by $\nu_y = \mu_B g B_y / hq$,[35]

$$S_x = (S_0/2) B_1 \Delta\nu \left[\frac{\Delta\nu \cos(2\pi\nu_1 t) + (\nu_1 - \nu_y)\sin(2\pi\nu_1 t)}{\Delta\nu^2 + (\nu_1 - \nu_y)^2} + \frac{\Delta\nu \cos(2\pi\nu_1 t) - (\nu_1 - \nu_y)\sin(2\pi\nu_1 t)}{\Delta\nu^2 + (\nu_1 - \nu_y)^2} \right], \tag{12}$$

where $\Delta\nu = 1/T_2$.

The data in Fig. 10 illustrate the sensitivity of our magnetometer to small oscillating fields on the order of pT in the presence of bias fields up to around 0.25 μT. Figure 10(a) shows the intensity of the NMR signal for ^{1}H Larmor precession in water over the frequency range 1-10 Hz (approximately 0–0.25 μT). For each data point, it was necessary to (approximately) compensate for the much stronger magnetometer response to the bias field so that the voltage of the photodiodes did not "clip" out of the range where they could be measured. The overall profile fits to an absorptive Lorentzian line shape centered near zero frequency, consistent with Eq. (12) for $|\nu_1| = |\gamma_{\mathrm{H}} B_y / 2\pi| \ll |\nu_y|$. Although there is a rapid loss of sensitivity with increasing bias field, the Larmor precession is easily detected over the 0-10 Hz region, enabling us to execute the field-zeroing protocol described earlier in this section and the near-zero-field NMR spectroscopy described in Sec. II. The data in Fig. 10(b) represent the magnetometer response to a 4.4 pT, 100 Hz test field over the same range of bias fields. The center of the Lorentzian is shifted away from zero field since the magnitude of the signal frequency ν_1 is now comparable with that of ν_y.

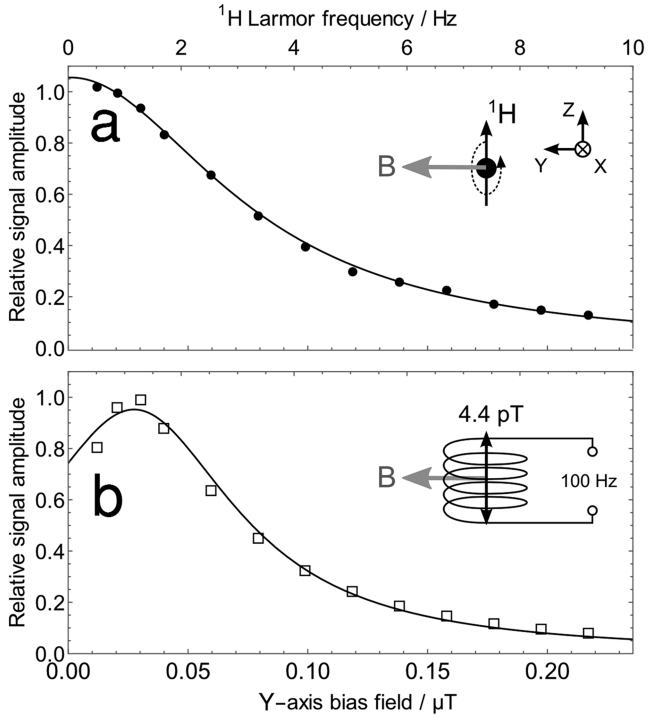

FIG. 10. Magnetometer sensitivity plotted measured as a function of a magnetic bias field along the y axis. Data points represent the amplitude of the detected signals originating from (a, circles •) ^{1}H spin precession in a 0.1 mL sample of tap water; (b, squares □) a 4.4 pT, 100 Hz test signal oscillating along the z axis. The magnetometer detects the component of the field along the z axis. Curve shapes are consistent with Eq. (12) and explained in the main text.

IV. SUMMARY AND OUTLOOK

We have described the setup and characterization of an instrument for detecting NMR signals in magnetic fields below $\approx 10^{-7}$ T, which we refer to as the ZULF regime. The key stages of the NMR experiment were reviewed: sample prepolarization, signal encoding using pulsed magnetic fields, and finally optical detection via magneto-optical rotation near the ^{87}Rb D1 transition in a SERF ^{87}Rb-vapor magnetometer. The instrument is used for direct measurements of nuclear spin-spin couplings and the Larmor precession near zero field. Indirect measurements of NMR up to fields of a few mT can also be made with high sensitivity, which includes NMR in earth's field.[53] The whole instrument is relatively inexpensive, compact and easy to maintain compared with the traditional NMR apparatus. As the techniques based on SERF magnetometers become mature, we expect the practical realization of many promising NMR applications, where the sensitivity or cost of low-field detection has hitherto been prohibitive. Examples include the characterization of fluids confined in pores, porous metals,[101] emulsions, and other inhomogeneous materials, the proposed measurement of antisymmetric spin-spin-coupling tensors in chiral molecules,[102] and the use of spin decoupling techniques for multidimensional spectroscopy.[81] While the examples presented here focus upon detection of NMR in liquid-state samples, the techniques are also applicable to other phases of matter, including gases and solids.

Although SERF alkali magnetometry techniques continue to be refined, fundamental sensitivity limits are close to being reached. At this stage, the molar sensitivity of ZULF NMR still remains several orders of magnitude below the state-of-the-art portable NMR instrumentation based on coil induction even at signal frequencies as low as 1 MHz. Room-temperature pre-polarization of samples around 1-2 T does not produce sufficient signal intensity for ZULF NMR to be used for routine analyses of organic molecules in mM concentration, even with full ^{13}C isotopic enrichment. However, this limitation can be overcome by techniques that produce a much higher starting polarization, for instance parahydrogen-induced polarization.[76–78] Dynamic nuclear polarization (DNP) is another experimental strategy for producing order-of-unity nuclear spin polarization in liquids, promising signal strength enhancement by a factor 10^5-10^6.[103–105] Another interesting future direction of ZULF NMR is extending the techniques to a single-molecule level using magnetometers based on single NV centers in diamond that have already demonstrated single-spin NMR capabilities, though not at ZULF.[106] This will take the technique to an unbeatable range of mass sensitivity and is ideal for stochastic polarization. The same may be true for magnetic resonance imaging (MRI). We note that only one decade since the first demonstration of ZULF NMR with atomic magnetometers,[28] several studies have demonstrated MRI, assisted by remote detection,[101,107,108] extended-cell and flux-transformer strategies,[109,110] although the alkali-vapor magnetometer and/or spatial encoding is used at higher magnetic fields on the order of mT and not in the ZULF/SERF regime. At present, SQUID magnetometry is preferred for larger spatial fields-of-view (e.g., imaging medical/physiological subjects), mainly because the technology is more mature.[16,46,111] As the alkali-vapor, SQUID and NV-diamond magnetometers continue to undergo a rapid stage of development and advance, including in ZULF, it is expected that the scenes will change dramatically over the coming years.

ACKNOWLEDGMENTS

We are grateful to M. P. Ledbetter for his critically important contribution in the development of the apparatus and techniques described in this paper. This material is based upon work supported by the National Science Foundation under Grant No. CHE-1308381 (authors D.B. and A.P.) and by the European Commission under the Marie Curie International Outgoing Fellowship Programme under Grant Agreement No. FP7-625054 ODMR-CHEM (author M.C.D.T.). S.P. acknowledges the support from the Polish Science Centre within the Opus Programme. The opinions, findings, and conclusions or recommendations expressed in this material are those of the authors and do not necessarily reflect the views of the National Science Foundation, Cambridge University, or the European Commission.

[1]H. D. W. Hill and G. A. Gray, "Spectrometers: A general overview," eMagRes (published online, 2011).
[2]S. Sýkora, "NMR sensitivity: Novel approaches and perspectives" (published online, 2005).
[3]N. Iriguchi, "The power sensitivity of magnetic resonance experiments," J. Appl. Phys. **73**, 2956–2957 (1993).
[4]A. Abragam, *The Principles of Nuclear Magnetism* (Clarendon Press, Oxford, 1961).

[5]D. I. Hoult and R. E. Richards, "The signal-to-noise ratio of the nuclear magnetic resonance experiment," J. Magn. Reson. **24**, 71–85 (1976).
[6]D. I. Hoult and P. C. Lauterbur, "The sensitivity of the zeugmatographic experiment involving human samples," J. Magn. Reson. **34**, 425–433 (1979).
[7]D. I. Hoult, *Sensitivity of the NMR Experiment* (eMagRes, John Wiley and Sons, Ltd., 2007).
[8]R. Freeman, "Selective excitation in high-resolution NMR," Chem. Rev. **91**, 1397–1412 (1991).
[9]P. Styles and N. F. Soffe, "A high-resolution NMR probe in which the coil and preamplifier are cooled with liquid helium," J. Magn. Reson. **60**, 397–404 (1984).
[10]G. E. Martin, "Small-volume and high-sensitivity NMR probes," Ann. Rep. NMR Spectrosc. **56**, 1–96 (2005).
[11]M. Lacey, R. Subramanian, D. L. Olson, A. G. Webb, and J. V. Sweedler, "High-resolution NMR spectroscopy of sample volumes from 1 nL to 1 μL," Chem. Rev. **99**, 3133–3152 (1999).
[12]R. McDermott, A. H. Trabesinger, M. Muck, E. Hahn, A. Pines, and J. Clarke, "Liquid-state NMR and scalar couplings in micro-tesla magnetic fields," Science **295**, 2247–2249 (2002).
[13]A. M. Thayer and A. Pines, "Zero-field NMR," Acc. Chem. Res. **20**, 47–53 (1987).
[14]D. B. Zax, A. Bielecki, K. W. Zilm, A. Pines, and D. Weitekamp, "Zero-field NMR and NQR," J. Chem. Phys. **83**, 4877–4905 (1985).
[15]J. W. Blanchard, T. F. Sjolander, J. P. King, M. P. Ledbetter, E. H. Levine, V. S. Bajaj, D. Budker, and A. Pines, "Measurement of untruncated nuclear spin interactions via zero- to ultralow-field nuclear magnetic resonance," Phys. Rev. B **92**, 220202(R) (2015).
[16]M. Mößle, S.-I. Han, W. R. Myers, S.-K. Lee, N. Kelso, M. Hatridge, A. Pines, and J. Clarke, "SQUID-detected microtesla MRI in the presence of metal," J. Magn. Reson. **179**, 146–151 (2006).
[17]R. Freedman, V. Anand, B. Grant, K. Ganesan, P. Tabrizi, R. Torres, D. Catina, D. Ryan, C. Borman, and C. Crueckl, "A compact high-performance low-field NMR apparatus for measurements on fluids at very high pressures and temperatures," Rev. Sci. Instrum. **85**, 025102 (2014).
[18]M. Emondts, M. P. Ledbetter, S. Pustelny, T. Theis, B. Patton, J. W. Blanchard, M. Butler, D. Budker, and A. Pines, "Long-lived heteronuclear spin singlet states in liquids at a zero magnetic field," Phys. Rev. Lett. **112**, 077601 (2014).
[19]J. W. Blanchard and D. Budker, "Zero- to ultralow-field NMR," eMagRes **5**, 1395 (2017).
[20]M. P. Ledbetter, C. W. Crawford, A. Pines, D. E. Wemmer, S. Knappe, J. Kitching, and D. Budker, "Optical detection of NMR J-spectra at zero magnetic field," J. Magn. Reson. **199**, 25–29 (2009).
[21]M. P. Ledbetter, T. Theis, J. W. Blanchard, H. Ring, P. J. Ganssle, S. Appelt, B. Blumich, A. Pines, and D. Budker, "Near-zero-field nuclear magnetic resonance," Phys. Rev. Lett. **107**, 107601 (2011).
[22]M. P. Ledbetter and D. Budker, "Zero-field nuclear magnetic resonance," Phys. Today **66**(4), 44 (2013).
[23]M. Butler, M. P. Ledbetter, T. Theis, J. W. Blanchard, D. Budker, and A. Pines, "Multiplets at zero magnetic field: The geometry of zero-field NMR," J. Chem. Phys. **138**, 184202–184215 (2013).
[24]J. W. Blanchard, M. P. Ledbetter, T. Theis, M. Butler, D. Budker, and A. Pines, "High-resolution zero-field NMR J-spectroscopy of aromatic compounds," J. Am. Chem. Soc. **135**, 3607–3612 (2013).
[25]T. Theis, J. W. Blanchard, M. Butler, M. P. Ledbetter, D. Budker, and A. Pines, "Chemical analysis using J-coupling multiplets in zero-field NMR," Chem. Phys. Lett. **580**, 160–165 (2013).
[26]J. E. Lenz, "A review of magnetic sensors," Proc. IEEE **78**, 973–989 (1990).
[27]I. K. Kominis, T. W. Kornack, J. C. Alfred, and M. V. Romalis, "A subfemtotesla multichannel atomic magnetometer," Nature **422**, 596–599 (2003).
[28]I. M. Savukov and M. V. Romalis, "NMR detection with an atomic magnetometer," Phys. Rev. Lett. **94**, 123001 (2005).
[29]I. M. Savukov, S. J. Seltzer, and M. V. Romalis, "Detection of NMR signals with a radio-frequency atomic magnetometer," J. Magn. Reson. **185**, 214–220 (2007).
[30]M. P. Ledbetter, I. M. Savukov, V. M. Acosta, D. Budker, and M. V. Romalis, "Spin-exchange-relaxation-free magnetometry with Cs vapor," Phys. Rev. A **77**, 033408 (2008).
[31]G. Bevilacqua, V. Biancalana, Y. Dancheva, and L. Moi, "All-optical magnetometry for NMR detection in a micro-tesla field an unshielded environment," J. Magn. Reson. **201**, 222–229 (2009).
[32]V. Tiporlini and K. Alameh, "High sensitivity optically pumped quantum magnetometer," Sci. World J. **2013**, 858379.
[33]D. Budker and M. V. Romalis, "Optical magnetometry," Nat. Phys. **3**, 227–234 (2007).
[34]D. Budker, W. Gawlik, D. F. Kimball, S. M. Rochester, V. V. Yashchuk, and A. Weis, "Resonant nonlinear magneto-optical effects in atoms," Rev. Mod. Phys. **74**, 1153–1201 (2002).
[35]*Optical Magnetometry*, edited by D. Budker and D. F. Jackson Kimball (Cambridge University Press, 2013), ISBN: 1107010357.
[36]S. Seltzer, "Developments in alkali-metal atomic magnetometry," Ph.D. thesis, Princeton University, 2008.
[37]W. Happer and H. Tang, "Spin-exchange shift and narrowing of magnetic resonance lines in optically pumped alkali vapors," Phys. Rev. Lett. **31**, 273–276 (1973).
[38]W. Happer and A. C. Tam, "Effect of rapid spin exchange on the magnetic resonance spectrum of alkali vapors," Phys. Rev. A **16**, 1877–1891 (1977).
[39]I. M. Savukov and M. V. Romalis, "Effects of spin-exchange collisions in a high-density alkali-metal vapor in low magnetic fields," Phys. Rev. A **71**, 023405 (2005).
[40]J. C. Allred, R. N. Lyman, T. W. Kornack, and M. V. Romalis, "High-sensitivity atomic magnetometer unaffected by spin-exchange relaxation," Phys. Rev. Lett. **89**, 130801 (2002).
[41]Y. S. Greenberg, "Application of superconducting quantum interference devices to nuclear magnetic resonance," Rev. Mod. Phys. **70**, 175–222 (1998).
[42]L. J. Friedman, A. K. M. Wennberg, S. N. Ytterboe, and H. M. Bozler, "Direct detection of low-frequency NMR using a dc SQUID," Rev. Sci. Instrum. **57**, 410 (1986).
[43]L. Q. Qiu, Y. Zhang, H. J. Krause, A. I. Braginski, S. Tanaka, and A. Offenhausser, "High-performance low-field NMR utilizing a high- T_c rf SQUID," IEEE Trans. Appl. Supercond. **19**, 831–834 (2009).
[44]M. P. Augustine, D. M. TonThat, and J. Clarke, "SQUID detected NMR and NQR," Solid State NMR **11**, 139–156 (1998).
[45]N. Q. Fan, M. B. Heaney, J. Clarke, D. Newitt, L. L. Wald, E. L. Hahn, A. Bielecki, and A. Pines, "Nuclear magnetic resonance with dc SQUID preamplifiers," IEEE Trans. Magn. **25**, 1193–1199 (1989).
[46]R. H. Kraus, Jr., M. Espy, P. Magnelind, and P. Vogelov, *Ultra-Low-Field Nuclear Magnetic Resonance: A New MRI Regime* (Oxford University Press, New York, 2014).
[47]M. Espy, A. N. Matlachov, P. Vogelov, and R. H. Kraus, Jr., "SQUID-based simultaneous detection of NMR and biomagnetic signals at ultra-low magnetic fields," IEEE Trans. Appl. Supercond. **15**, 635–639 (2005).
[48]A. N. Matlashov, L. J. Schultz, M. A. Espy, R. H. Kraus, I. M. Savukov, P. L. Volegov, and C. J. Wurden, "SQUIDs vs. induction coils for ultra-low field nuclear magnetic resonance: Experimental and simulation comparison," IEEE Trans. Appl. Supercond. **21**, 465–468 (2011).
[49]M. P. Ledbetter, I. M. Savukov, D. Budker, V. Shah, S. Knappe, J. Kitching, D. J. Michalak, S. Xu, and A. Pines, "Zero-field remote detection of NMR with a microfabricated atomic magnetometer," Proc. Natl. Acad. Sci. U. S. A. **105**, 2286–2290 (2008).
[50]V. Shah, S. Knappe, P. D. D. Schwindt, and J. Kitching, "Subpicotesla atomic magnetometry with a microfabricated vapour cell," Nat. Photon. **1**, 649–652 (2007).
[51]R. Jiminéz-Martinez, D. J. Kennedy, M. Rosenbluh, E. A. Donley, S. Knappe, S. J. Seltzer, H. L. Ring, V. S. Bajaj, and J. Kitching, "Optical hyperpolarization and NMR detection of 129Xe on a microfluidic chip," Nat. Commun. **5**, 3908 (2014).
[52]I. M. Savukov, V. S. Zotev, P. L. Volegov, M. A. Espy, A. N. Matlashov, J. J. Gomez, and R. H. Kraus, Jr., "MRI with an atomic magnetometer suitable for practical imaging applications," J. Magn. Reson. **199**, 188–191 (2009).
[53]P. J. Ganssle, H. D. Shin, S. J. Seltzer, V. S. Bajaj, M. P. Ledbetter, D. Budker, S. Knappe, J. Kitching, and A. Pines, "Ultra-low-field NMR relaxation and diffusion measurements using an optical magnetometer," Angew. Chem., Int. Ed. **53**, 9766–9770 (2014).
[54]V. V. Yashchuk, J. Granwehr, D. F. Kimball, S. M. Rochester, A. H. Trabesinger, J. T. Urban, D. Budker, and A. Pines, "Hyperpolarized xenon nuclear spins detected by optical atomic magnetometry," Phys. Rev. Lett. **93**, 160801 (2004).
[55]A. Wilzewski, S. Afach, J. W. Blanchard, and D. Budker, "A method for measurement of spin-spin couplings with sub-mHz precision using zero- to ultralow-field nuclear magnetic resonance," J. Magn. Reson. (published online, 2017).

[56]Y. Shimizu, J. W. Blanchard, S. Pustelny, G. Saielli, A. Bagno, M. P. Ledbetter, D. Budker, and A. Pines, "Zero-field nuclear magnetic resonance spectroscopy of viscous liquids," J. Magn. Reson. **250**, 1–6 (2015).
[57]P. D. D. Schwindt and C. N. Johnson, "Atomic magnetometer for human magnetoencephalography," Sandia National Laboratories Report SAND 2010–8443, 2010, http://prod.sandia.gov/techlib/access-control.cgi/2010/108443.pdf.
[58]C. A. Baker, D. D. Doyle, P. Geltenbort, K. Green, M. G. D. van der Grinten, P. G. Harris, P. Iaydjiev, S. N. Ivanov, D. J. R. May, J. M. Pendlebury, J. D. Richardson, D. Shiers, and K. F. Smith, "Improved experimental limit on the electric dipole moment of the neutron," Phys. Rev. Lett. **97**, 131801 (2006).
[59]A. Maul, P. Blümler, W. Heil, A. Nikiel, E. Otten, A. Petrich, and T. Schmidt, "Spherical fused silica cells filled with pure helium for nuclear magnetic resonance magnetometry," Rev. Sci. Instrum. **87**, 015103 (2016).
[60]T. W. Kornack, R. K. Ghosh, and M. V. Romalis, "Nuclear spin gyroscope based on an atomic magnetometer," Phys. Rev. Lett. **95**, 230801 (2005).
[61]E. A. Donley, "Nuclear magnetic resonance gyroscopes," in *IEEE Sensors Conference* (IEEE, 2010), pp. 17–22.
[62]S. Appelt, F. W. Häsing, U. Sieling, A. Gordji Nejad, S. Glöggler, and B. Blümich, "Paths from weak to strong coupling in NMR," Phys. Rev. A **81**, 023420 (2010).
[63]J. Bernarding, G. Buntkowsky, S. Macholl, S. Hartwig, M. Burghoff, and L. Trahms, "J-coupling nuclear magnetic resonance spectroscopy of liquids in nT fields," J. Am. Chem. Soc. **128**, 714–715 (2006).
[64]G. Bevilacqua, V. Biancalana, A. B.-A. Baranga, Y. Dancheva, and C. Rossi, "Microtesla NMR J-coupling spectroscopy with an unshielded atomic magnetometer," J. Magn. Reson. **263**, 65–70 (2016).
[65]L. Trahms and M. Burghoff, "NMR at very low fields," Magn. Reson. Imaging **28**, 1244–1250 (2010).
[66]J. H. Shim, S.-J. Lee, S.-m. Hwang, K.-K. Yu, and K. Kim, "Two-dimensional NMR spectroscopy of methanol at less than 5 microtesla," J. Magn. Reson. **246**, 4–8 (2014).
[67]T. W. Kornack, S. J. Smullin, S.-K. Lee, and M. V. Romalis, "A low-noise ferrite magnetic shield," Appl. Phys. Lett. **90**, 223501 (2007).
[68]F. Thiel, A. Schnabel, S. Knappe-Grüneberg, D. Stollfuß, and M. Burghoff, "Demagnetization of magnetically shielded rooms," Rev. Sci. Instrum. **78**, 035106 (2007).
[69]V. Biancalana, Y. Dancheva, and L. Stiaccini, "Note: A fast pneumatic sample-shuttle with attenuated shocks," Rev. Sci. Instrum. **85**, 036104 (2014).
[70]C. R. Bowers and D. P. Weitekamp, "Transformation of symmetrization order to nuclear-spin magnetization by chemical reaction and nuclear magnetic resonance," Phys. Rev. Lett. **57**, 2645–2648 (1986).
[71]C. R. Bowers and D. P. Weitekamp, "Parahydrogen and synthesis allow dramatically enhanced nuclear alignment," J. Am. Chem. Soc. **109**, 5541–5542 (1987).
[72]R. W. Adams, J. A. Aguilar, K. D. Atkinson, M. J. Cowley, P. I. Elliott, S. B. Duckett, G. G. Green, I. G. Khazal, J. Lopez-Serrano, and D. C. Williamson, "Reversible interactions with para-hydrogen enhance NMR sensitivity by polarization transfer," Science **323**, 1708–1711 (2009).
[73]J. F. P. Colell, A. J. W. Logan, Z. Zhou, R. V. Shchepin, D. A. Barskiy, G. X. Ortiz, Jr., Q. Wang, S. J. Malcolmson, E. Y. Chekmenev, W. S. Warren, and T. Theis, "Generalizing, extending, and maximizing nitrogen-15 hyperpolarization induced by parahydrogen in reversible exchange," J. Phys. Chem. C **121**, 6626 (2017).
[74]T. Theis, M. L. Truong, A. M. Coffrey, R. V. Shchepin, K. W. Waddell, F. Shi, B. M. Goodson, W. S. Warren, and E. Y. Chekmenev, "Microtestla SABRE enables 10% nitrogen-15 nuclear spin polarization," J. Am. Chem. Soc. **137**, 1404–1407 (2015).
[75]V. V. Zhivonitko, I. V. Skovpin, and I. V. Koptyug, "Strong ^{31}P nuclear spin hyperpolarization produced via reversible chemical interaction with parahydrogen," Chem. Commun. **51**, 2506–2509 (2015).
[76]T. Theis, P. Ganssle, G. Kervern, S. Knappe, J. Kitching, M. P. Ledbetter, D. Budker, and A. Pines, "Parahydrogen-enhanced zero-field nuclear magnetic resonance," Nat. Phys. **7**, 571–575 (2011).
[77]M. Butler, G. Kervern, T. Theis, M. P. Ledbetter, P. J. Ganssle, J. W. Blanchard, D. Budker, and A. Pines, "Parahydrogen-induced polarization at zero magnetic field," J. Chem. Phys. **138**, 234201 (2013).
[78]T. Theis, M. P. Ledbetter, G. Kervern, J. W. Blanchard, P. J. Ganssle, M. Butler, H. D. Shin, D. Budker, and A. Pines, "Zero-field NMR enhanced by parahydrogen in reversible exchange," J. Am. Chem. Soc. **134**, 3987–3990 (2012).
[79]C. J. Lee, D. Suter, and A. Pines, "Theory of multiple-pulse NMR at low and zero fields," J. Magn. Reson. **75**, 110–124 (1987).
[80]A. Llor, Z. Olejniczak, J. Sachleben, and A. Pines, "Scaling and time reversal of spin couplings in zero-field NMR," Phys. Rev. Lett. **67**, 1989–1992 (1991).
[81]T. F. Sjolander, M. C. D. Tayler, A. Kentner, D. Budker, and A. Pines, "Homonuclear *J*-coupling spectroscopy using two-dimensional nuclear magnetic resonance at zero field," J. Phys. Chem. Lett. **8**, 1512 (2017).
[82]M. C. D. Tayler, T. F. Sjolander, A. Pines, and D. Budker, "Nuclear magnetic resonance at millitesla fields using a zero-field spectrometer," J. Magn. Reson. **270**, 35–39 (2016).
[83]T. F. Sjolander, M. C. D. Tayler, D. Budker, and A. Pines, "Transition-selective pulses in zero-field nuclear magnetic resonance," J. Phys. Chem. A **120**, 4343–4348 (2016).
[84]J. DuPont-Roc, S. Haroche, and C. Cohen-Tannoudji, "Detection of very weak magnetic fields (10^{-9} gauss) by ^{87}Rb zero-field level crossing resonances," Phys. Lett. A **28**, 638–639 (1969).
[85]C. Cohen-Tannoudji, J. DuPont-Roc, S. Haroche, and F. Laloë, "Detection of the static magnetic field produced by the oriented nuclei of optically pumped ^{3}He gas," Phys. Rev. Lett. **22**, 758–760 (1969).
[86]W. E. Bell and A. L. Bloom, "Optically driven spin precession," Phys. Rev. Lett. **6**, 280 (1961).
[87]W. E. Bell and A. L. Bloom, "Optical detection of magnetic resonance in alkali metal vapor," Phys. Rev. **107**, 1559 (1957).
[88]I. Savukov, "Ultra-sensitive optical atomic magnetometers and their applications," in *Advances in Optical and Photonic Devices*, edited by K. Y. Kim (InTech., 2010), Chap. 17, p. 352, ISBN: 978-953-7619-76-3.
[89]E. B. Alexandrov, M. Auzinsh, D. Budker, D. F. Kimball, S. M. Rochester, and V. V. Yashchuk, "Dynamic effects in nonlinear magneto-optics of atoms and molecules: Review," J. Opt. Soc. Am. B **22**, 7–20 (2005).
[90]R. Srinivasan, "Nonlinear magneto-optical rotation—A possible tool for sensitive magnetometry," Curr. Sci. **92**, 298–307 (2007), available at http://www.jstor.org/stable/24096724.
[91]D. Macaluso and O. M. Corbino, "Sopra una nuova azione che la luce subisce attraversando alcuni vapori metallici in un campo magnetico," Il Nuovo Cimento **8**, 257 (1898).
[92]D. Macaluso and O. M. Corbino, "Sulla relazione tra il fenomeno di Zeemann e la rotazione magnetica anomala del piano di polarizzazione della luce," Il Nuovo Cimento **9**, 384 (1898).
[93]P. Zeeman, "The effect of magnetisation on the nature of light emitted by a substance," Nature **55**, 347 (1897).
[94]W. Happer, "Optical pumping," Rev. Mod. Phys. **44**, 169–249 (1972).
[95]W. Happer and B. S. Mathur, "Effective operator formalism in optical pumping," Phys. Rev. **163**, 12–25 (1967).
[96]T. G. Walker and W. Happer, "Spin-exchange optical pumping of noble-gas nuclei," Rev. Mod. Phys. **69**, 629–642 (1997).
[97]S. Kadlecek, L. W. Anderson, and T. G. Walker, "Measurement of potassium-potassium spin relaxation cross sections," Nucl. Instrum. Methods Phys. Res., Sect. A **402**, 208–211 (1998).
[98]A. F. Molisch and B. P. Oehry, *Radiation Trapping in Atomic Vapors*, Oxford Science Publications (Clarendon Press, Oxford, 1998), ISBN: 0198538669.
[99]D. A. Steck, Rubidium-87 D-line data, online at, http://steck.us/alkalidata revision 2.1.5, 2015.
[100]V. Shah, G. Vasilakis, and M. V. Romalis, "High-bandwidth atomic magnetometry with continuous quantum nondemolition measurements," Phys. Rev. Lett. **104**, 013601 (2010).
[101]S. Xu, E. Harel, D. J. Michalak, C. W. Crawford, D. Budker, and A. Pines, "Flow in porous metallic materials: A magnetic resonance imaging study," J. Magn. Reson. Imaging **28**, 1299–1302 (2008).
[102]J. P. King, T. F. Sjolander, and J. W. Blanchard, "Antisymmetric couplings enable direct observation of chirality in nuclear magnetic resonance spectroscopy," J. Phys. Chem. Lett. **8**, 710 (2016).
[103]A. Abragam and M. Goldman, "Principles of dynamic nuclear polarisation," Rep. Prog. Phys. **41**, 395 (1978).
[104]T. Wenckebach, *Essentials of Dynamic Nuclear Polarization*, 1st ed. (Spindrift Publications, 2016), ISBN: 978–9075541182.
[105]W. Köckenberger, "Dissolution dynamic nuclear polarization," eMagRes **3**, 161–170 (2014).
[106]I. Lovchinsky, A. O. Sushkov, E. Urbach, N. P. de Leon, S. Choi, K. De Greve, R. Evans, R. Gertner, E. Bersin, C. Müller, L. McGuinness, F. Jelezko, R. L. Walsworth, H. Park, and M. D. Lukin, "Nuclear magnetic resonance detection and spectroscopy of single proteins using quantum logic," Science **351**, 836–841 (2016).

[107]S. Xu, V. V. Yashchuk, M. H. Donaldson, S. M. Rochester, D. Budker, and A. Pines, "Magnetic resonance imaging with an optical atomic magnetometer," Proc. Natl. Acad. Sci. U. S. A. **103**, 12668–12671 (2006).

[108]S. Xu, C. W. Crawford, S. M. Rochester, V. V. Yashchuk, D. Budker, and A. Pines, "Submillimeter-resolution magnetic resonance imaging at the Earth's magnetic field with an atomic magnetometer ," Phys. Rev. A **78**, 013404 (2006).

[109]I. Savukov and T. Karaulanov, "Anatomical MRI with an atomic magnetometer," J. Magn. Reson. Imaging **231**, 39–45 (2013).

[110]I. Savukov, T. Karaulanov, C. J. V. Wurden, and L. Schultz, "Non-cryogenic ultra-low field MRI of wrist-forearm area," J. Magn. Reson. Imaging **233**, 103–106 (2013).

[111]J. Clarke, M. Hatridge, and M. Mößle, "SQUID-detected magnetic resonance imaging in microtesla fields," Annu. Rev. Biomed. Eng. **9**, 389–413 (2007).